

Magneto-transport in closed and open mesoscopic loop structures: A review

Paramita Dutta^{1,*} and Santanu K. Maiti^{2,†}

¹*Condensed Matter Physics Division, Saha Institute of Nuclear Physics,
Sector-I, Block-AF, Bidhannagar, Kolkata-700 064, India*

²*Physics and Applied Mathematical Unit, Indian Statistical Institute,
203 Barrackpore Trunk Road, Kolkata-700 108, India*

Magneto-transport properties in closed and open loop structures are carefully reviewed within a tight-binding formalism. A novel mesoscopic phenomenon where a non-vanishing current is observed in a conducting loop upon the application of an Aharonov-Bohm flux ϕ and we explore its behavior in the aspects of quantum phase coherence, electron-electron correlation and disorder. The essential results are analyzed in three different parts. First, we examine the behavior of persistent current in different branches of a zigzag carbon nanotube within a Hartree-Fock mean field approach using the second quantized formulation. The phase reversal of persistent current in several branches as a function of Hubbard interaction is found to exhibit interesting patterns. Our numerical results suggest a filling-dependent metal-insulator transition in a zigzag carbon nanotube. Next, we address the behavior of persistent current in an ordered-disordered separated nanotube keeping in mind a possible experimental realization of shell-doped nanowire which can provide a strange electronic behavior rather than uniformly doped nanowires. Finally, we focus our attention on the behavior of persistent current in an open loop geometry where we clamp an ordered binary alloy ring between two ideal semi-infinite electrodes to make an electrode-ring-electrode bridge. From our investigation we propose that under suitable choices of the parameter values the system can act as a p -type or an n -type semiconductor.

PACS numbers: 73.23.-b, 73.23.Ra., 71.23.An

I. INTRODUCTION

The abundant progress in nano-science and technology has stimulated us to fabricate different artificial nano-structures over the last few decades whose dimensions are comparable to and even smaller than the mean free paths or wavelengths of electrons such that they can move through the samples without randomizing their phase memories¹. The manifestation of phase coherence length is one of the most striking aspects in the mesoscopic regime which can be obtained by lowering the temperature of the samples below sub-Kelvin temperatures since the scatterings due to electron-electron and electron-phonon interactions are highly suppressed in this temperature regime. Such experimentally accessible low-temperatures also make the system energy levels behave like discrete states which play a pivotal role in appearing several quantum-mechanical phenomena. Therefore, a mesoscopic system which can be modeled as a phase-coherent elastic scatterer² provides us the opportunity to explore various novel quantum-mechanical effects beyond the atomic realm³. The experimental realization of different quantum-mechanical incidents like, universal conductance fluctuations, non-local current-voltage relationship, new Onsager reciprocity relations, Coulomb blockade in micro-tunnel junctions⁴⁻⁸, Anderson localization⁹, quantum Hall-effect¹⁰, Aharonov-Bohm (AB) oscillations¹¹⁻¹⁴, to name a few, has raised the popularity of the mesoscopic world among the scientists and engineers. Another reason behind this popularity can be attributed to the tailor-made geometries which look very simple but have high potential from the application per-

spective. In addition, several other fluctuation patterns of the conductance are easily reproducible simply by tuning external parameters like, magnetic field, electric field, Fermi level, etc.

The existence of dissipationless current, the so-called persistent current, in a mesoscopic normal metal ring pierced by an AB flux ϕ is one of such remarkable effects which reveals the importance of phase coherence of electronic wave functions in low-dimensional quantum systems. The alluring question of persistent current in normal-metal rings threaded an AB flux was first explored during 1960's¹⁵. Later, in 1983, Büttiker *et al.* have revived the interest regarding this topic¹⁶. They have predicted that a small isolated normal metal ring penetrated by a slowly varying magnetic flux carries an equilibrium current which does not decay and circulates within the sample. But its experimental realization was somewhat difficult because at that time it was a challenging task to confine magnetic flux in such a small region like nanoscale ring. However, a few years later Levy *et al.*¹⁷ have given first experimental evidence of persistent current in a mesoscopic metallic ring. They have observed the oscillations with period $\phi_0/2$ ($\phi_0 = ch/e$, the elementary flux-quantum) while measuring persistent current in an ensemble of 10^7 independent Cu rings. Similar oscillations with period $\phi_0/2$ have also been reported not only for an ensemble of disconnected 10^5 Ag rings¹⁸ but also for an array of 10^5 isolated GaAs-AlGaAs rings¹⁹. Later, many other theoretical²⁰⁻²⁹ as well as experimental³⁰⁻³³ attempts have been done to explore the actual mechanisms of persistent current in single-channel rings and multi-channel cylinders. However, a contro-

versy still persists among the experimental observations and theoretical estimates of persistent current amplitudes. All the experimentally measured current amplitudes were found to be one and two orders of magnitude larger than the theoretically predicted results, except in the case of nearly ballistic GaAs-AlGaAs rings³⁰ where ϕ_0 -periodic persistent currents have been observed with amplitude $I_0 \sim ev_F/L$ (v_F and L are the Fermi velocity and circumference of the ring, respectively), which is very close to the value obtained from the free electron theory at absolute zero temperature ($T = 0$ K). In a recent work, Bluhm *et al.*³³ have examined magnetic response of 33 individual cold mesoscopic gold rings, considering one ring at a time, using a scanning SQUID technique. Their results agree well with the theoretically estimated value²⁰ in a single ballistic ring³⁰ and an ensemble of 16 nearly ballistic rings³⁴. But, the amplitudes of persistent current in single-isolated-diffusive gold rings³⁵ are still two orders of magnitude larger than the theoretical calculations. This discrepancy initiated intense theoretical activity, and it is generally believed that the electron-electron correlation plays an important role in the disordered diffusive rings³⁶⁻³⁸. An explanation based on the perturbative calculation in presence of interaction and disorder has been proposed and it seems to give a quantitative estimate closer to the experimental results, but still it is less than the measured currents by an order of magnitude, and the interaction parameter used in the theory is not well understood physically.

The behavior of persistent current in an isolated loop geometry enclosing a magnetic flux is highly sensitive to the location of Fermi level of the system where the role of magnetic flux is essentially to destroy the time-reversal symmetry and as a result, the degeneracies among the current-carrying states get removed. Depending on the Fermi level and the direction of the magnetic flux current flows in either direction revealing diamagnetic or paramagnetic nature. Since the discovery persistent current have been studying in different kinds of mesoscopic loop structures. Among them single channel mesoscopic rings^{20,39} were mainly in the focus of attention in spite of having topological simplicity they carry a high potential from the application point of view. Not only single isolated rings but also array of such rings have been used to study the nature of persistent current. A very few works on multi-channel closed loop systems have been discussed⁴⁰⁻⁴². In case of multi-channel mesoscopic cylinders it has been noticed that the typical single-level current gets reduced with increasing number of conducting channels M . The correlations in the energy spectrum governs that the ratio of the total and single-level currents is proportional to \sqrt{M} ⁴⁰.

Similar to persistent current in such isolated closed loop geometries, the non-decaying charge current is also observed in open loop systems⁴³⁻⁵¹, where rings/cylinders are coupled to source and drain electrodes. In 1985, Büttiker has introduced a conceptually simple and elegant approach⁴³ to investigate the effect of

an electron reservoir on persistent current in a loop penetrated by a magnetic flux. The reservoir is considered as a source of dissipation and the inelastic scattering processes take place only within this reservoir to which the loop is attached via a single current lead while the other scatterings occur in the lead are assumed to be elastic. So, there exists a complete spatial separation between the elastic and inelastic scatterings. The reservoir being a sink of electrons maintained the chemical potential of the loop to a fixed value. This modifies the statistical mechanical treatment of the system to a different ensemble, the grand canonical ensemble where close systems (in absence of lead and reservoir) belong to canonical ensemble average. This establishes a remarkable difference between the study of closed and open loop systems from the statistical point of view. Experimental verification of persistent current in open system was first done by Mailly *et al.* in 1993³⁰. They have examined both closed and open systems and detected a periodic signal carrying the signature of persistent current which was in agreement with the theory. After those pioneering works last two decades have witnessed several approaches to reveal the properties of persistent currents in open systems. Unlike the behavior of the other physical quantity such as conductance, persistent current in open system is sensitive to the direction of the transport current and this property is helpful for recognizing this current from the other currents (noise) associated with experimental measurements. In open systems, persistent current can appear even in absence of external magnetic field⁵² as the lead-current, the current from the source to drain, plays the role of the driving force. Jayannavar *et al.*^{52,53} have shown theoretically the flow of persistent current in an open metallic loop connecting to two electron reservoirs. They have taken the lengths of the two arms of the loop unequal which results in a circulating current in the loop. Instead of setting the arm-lengths unequal one can also introduce any local scatterer anywhere in the geometry to establish a circular flow within the loop geometry in non-equilibrium situation. On the other hand, in an equilibrium condition i.e., when the chemical potentials of both leads are same, persistent current can still arise due to evanescent modes. In a work by Jayannavar *et al.* the phenomenon of persistent current due to two non-classical effects, AB effect and quantum mechanical tunneling has been studied in detail^{53,54}.

Although the studies involving persistent current in single-channel rings and multi-channel rings⁵⁵ or cylinders, both in the closed and open loop shapes, have already generated a wealth of literature there is still need to look deeper into the problem to address several significant issues those have not been well explored before as for examples the understanding of the distribution of persistent currents in different channels in presence of electron-electron interaction and disorder which inspect the net response of the full system and also the sensitivity of persistent current on disorder in partially disordered systems like shell-doped nanowires which can provide a un-

familiar electronic behavior rather than uniformly doped nanowires. In the present review we essentially concentrate on these issues.

In the first part we address magneto-transport properties in a zigzag carbon nanotube, formed by rolling up a graphite ribbon in the cylindrical form⁵⁶, with its detailed energy band structure in presence electron-electron interaction within a Hartree-Fock (HF) mean field approach using the second quantized formulation. Since the isolation of a single layer graphene by Novoselov *et al.*⁵⁷ intense and diverse research is going on to explore electronic transport in this system. Graphene, a single layer of carbon atoms tightly packed into a two-dimensional honey-comb lattice, has drawn attention of scientists in various disciplines due to its unconventional and fascinating electronic properties arising particularly from the linear dispersion relation around the Dirac points of the hexagonal Brillouin zone. These unique properties can be understood in terms of the Dirac Hamiltonian⁵⁸ since it actually describes the physics of electrons near the Fermi level of the undoped material. The carriers in graphene effectively behave as massless relativistic particles within a low energy range close to Fermi energy and these massless Dirac Fermions⁵⁹ evince various phenomena in this energy range. The bipartite character of the wonderful lattice structure of graphene strongly influences its intrinsic properties and makes graphene a wonderful testbed for quantum field theory and mathematical physics as well as condensed matter theory. In the last few years extensive studies on persistent current in carbon nanotubes have been performed and many interesting physical phenomena have been explored^{60–62}. Persistent current in a carbon nanotube is highly sensitive to its radius, chirality, deformation, etc. In a recent experiment it has also been observed that the Fermi energy of a carbon nanotube can be regulated nicely by means of electron or hole doping, which can induce a dramatic change in persistent current⁶². It is well established that in a conventional multi-channel mesoscopic cylinder electron transport strongly depends on the correlation among different channels as well as the shape of Fermi surface. Therefore, we might expect some interesting features of persistent current in a carbon nanotube due to its unique electronic structure. Here we discuss the behavior of persistent current in different branches together with the total current of a zigzag carbon nanotube in presence of an AB flux. Most of the works available in literature^{20,60–67} generally investigate magnetic response of the entire system, but a complete knowledge of magnetic response in individual branches provide much better insight to the problem⁶⁸. The phase reversal of persistent current in different branches as a function of electron-electron correlation is found to exhibit interesting pattern. Our detailed numerical analysis suggests a filling-dependent metal-insulator (MI) transition in a zigzag carbon nanotube.

In the second part, we concentrate on the behavior persistent current in an ordered-disordered separated nanotube considering a possible experimental realization of

shell-doped nanowires which may provide several unusual electronic behavior rather than uniformly doped nanowires and have potential applications in nanoscale electronic and optoelectronic devices.

In the last part we investigate persistent current together with average density of states (ADOS) in an open loop geometry where an ordered binary alloy ring threaded by a magnetic flux is clamped between two ideal semi-infinite metallic electrodes, commonly known as source and drain electrodes, followed by the characteristic properties of an isolated ordered binary alloy ring. Inclusion of some foreign atoms in anyone of the two arms of the ring provides some interesting patterns in ADOS and from our numerical analysis we propose that under suitable choices of the parameter values the system can act as a *p*-type or an *n*-type semiconductor.

Throughout the review we choose $c = e = h = 1$ for numerical calculations and restrict ourselves at absolute zero temperature.

II. MAGNETO-TRANSPORT IN A ZIGZAG CARBON NANOTUBE

This section is devoted to reveal the magnetic response of interacting electrons in a zigzag carbon nanotube enclosing a magnetic flux within a HF mean field approach. Following the description of energy spectra for

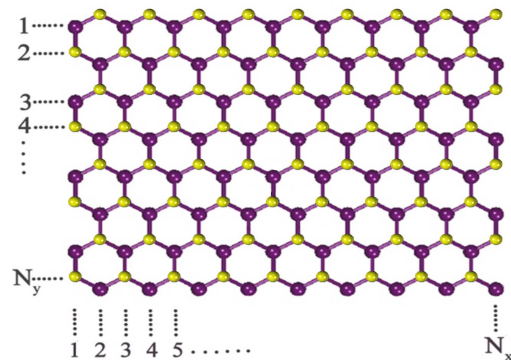


FIG. 1: (Color online). Schematic view of a zigzag graphite nano-ribbon with N_x and N_y number of atomic sites along the x and y directions, respectively.

both non-interacting and interacting cases we investigate the energy-flux characteristics, persistent current in individual branches of the system and also the net current of the entire system.

A. The model and the mean field scheme

We begin by referring to Fig. 1 where a graphite nano-ribbon of zigzag edges is shown. The filled magenta (large) and yellow (small) circles correspond to two different sub-lattices, namely, A and B, respectively. N_x

and N_y are the number of atomic sites along the x and y directions, respectively. In order to elucidate magnetic response of a nanotube we roll up the graphite ribbon along x direction using periodic boundary condition and allow to pass a magnetic flux ϕ (measured in unit of elementary flux quantum $\phi_0 = ch/e$) along the axis of the tube as shown in Fig. 2. Our model quantum system is illustrated by the nearest-neighbor tight-binding (TB) framework which captures most of the essential proper-

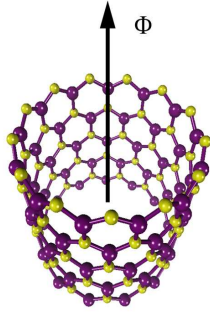


FIG. 2: (Color online). A graphite nanotube threaded by a magnetic flux Φ .

ties of the tube nicely^{69–72}. To incorporate the effect of electron-electron interaction in the Hamiltonian we employ a HF mean field approximation. In Wannier basis, the Hamiltonian of an zigzag nanotube takes the form,

$$\begin{aligned}
 H = & t \sum_{m,n,\sigma} \left(\mathbf{a}_{m,n,\sigma}^\dagger \mathbf{b}_{m-1,n,\sigma} e^{-i\theta} \right. \\
 & + \mathbf{a}_{m,n,\sigma}^\dagger \mathbf{b}_{m+1,n,\sigma} e^{i\theta} + \mathbf{a}_{m,n,\sigma}^\dagger \mathbf{b}_{m,n+1,\sigma} \left. \right) + \text{h.c.} \\
 & + U \sum_{m,n} \left(\mathbf{a}_{m,n,\uparrow}^\dagger \mathbf{a}_{m,n,\uparrow} \mathbf{a}_{m,n,\downarrow}^\dagger \mathbf{a}_{m,n,\downarrow} \right. \\
 & \left. + \mathbf{b}_{m+1,n,\uparrow}^\dagger \mathbf{b}_{m+1,n,\uparrow} \mathbf{b}_{m+1,n,\downarrow}^\dagger \mathbf{b}_{m+1,n,\downarrow} \right) \quad (1)
 \end{aligned}$$

where, $\mathbf{a}_{m,n,\sigma}^\dagger$ ($\mathbf{b}_{m,n,\sigma}^\dagger$) is the creation operator for an up spin or down spin electron of spin associated with

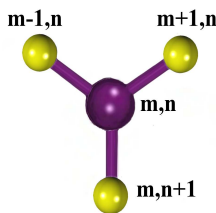


FIG. 3: (Color online). Schematic view of different atomic sites with their co-ordinates.

A (B) type of atoms at the position (m,n) and the corresponding annihilation operator is denoted by $a_{m,n}$ ($b_{m,n}$). t is the nearest-neighbor hopping integral and U is the strength of on-site Hubbard interaction. The coordinates of the lattice sites are denoted by two integers,

m and n . The site indexing is schematically shown in Fig. 3 for better viewing. The factor θ ($= 2\pi\phi/N_x$), the so-called Peierl's⁷³ phase factor, is introduced into the above Hamiltonian to incorporate the effect of magnetic flux applied along the axis of the tube.

Decoupling of interacting Hamiltonian: Using the generalized HF approach, the so-called mean-field approximation, we decouple the TB Hamiltonian into three different parts two of which correspond to two different values of σ , \uparrow and \downarrow , with modified site-energies. The decoupled Hamiltonian is expressed as,

$$\mathbf{H}_{\text{MF}} = \mathbf{H}_\uparrow + \mathbf{H}_\downarrow + \mathbf{H}_0 \quad (2)$$

where,

$$\begin{aligned}
 \mathbf{H}_\uparrow = & U \sum_{m,n} \left(\langle \mathbf{n}_{m,n,\downarrow}^a \rangle \mathbf{n}_{m,n,\uparrow}^a + \langle \mathbf{n}_{m+1,n,\downarrow}^b \rangle \mathbf{n}_{m+1,n,\uparrow}^b \right) \\
 & + t \sum_{m,n} \left(\mathbf{a}_{m,n,\uparrow}^\dagger \mathbf{b}_{m-1,n,\uparrow} e^{-i\theta} + \mathbf{a}_{m,n,\uparrow}^\dagger \mathbf{b}_{m+1,n,\uparrow} e^{i\theta} \right. \\
 & \left. + \mathbf{a}_{m,n,\uparrow}^\dagger \mathbf{b}_{m,n+1,\uparrow} + \text{h.c.} \right), \\
 \mathbf{H}_\downarrow = & U \sum_{m,n} \left(\langle \mathbf{n}_{m,n,\uparrow}^a \rangle \mathbf{n}_{m,n,\downarrow}^a + \langle \mathbf{n}_{m+1,n,\uparrow}^b \rangle \mathbf{n}_{m+1,n,\downarrow}^b \right) \\
 & + t \sum_{m,n} \left(\mathbf{a}_{m,n,\downarrow}^\dagger \mathbf{b}_{m-1,n,\downarrow} e^{-i\theta} + \mathbf{a}_{m,n,\downarrow}^\dagger \mathbf{b}_{m+1,n,\downarrow} e^{i\theta} \right. \\
 & \left. + \mathbf{a}_{m,n,\downarrow}^\dagger \mathbf{b}_{m,n+1,\downarrow} + \text{h.c.} \right), \\
 \mathbf{H}_0 = & -U \sum_{m,n} \left(\langle \mathbf{n}_{m,n,\uparrow}^a \rangle \langle \mathbf{n}_{m,n,\downarrow}^a \rangle \right. \\
 & \left. + \langle \mathbf{n}_{m+1,n,\uparrow}^b \rangle \langle \mathbf{n}_{m+1,n,\downarrow}^b \rangle \right). \quad (3)
 \end{aligned}$$

where, \mathbf{H}_\uparrow and \mathbf{H}_\downarrow represent the up-spin and down-spin Hamiltonians, respectively. \mathbf{H}_0 is a constant term which gives the energy shift. Here, $\mathbf{n}_{m,n,\sigma}^a$ and $\mathbf{n}_{m,n,\sigma}^b$ are the number operators associated with the A and B sites, respectively.

Self-consistent procedure: In order to get the energy eigenvalues of the interacting Hamiltonian we go through a self-consistent procedure considering initial guess values of $\langle \mathbf{n}_{m,n,\sigma}^a \rangle$ and $\langle \mathbf{n}_{m,n,\sigma}^b \rangle$. With these initial values, the up and down spin Hamiltonians are diagonalized numerically and a new set of values of $\langle \mathbf{n}_{m,n,\sigma}^a \rangle$ and $\langle \mathbf{n}_{m,n,\sigma}^b \rangle$ are calculated. These steps are repeated until a self-consistent solution is achieved.

Finding the ground state energy: After getting the self-consistent solution we determine the ground state energy (E_0) at absolute zero temperature ($T = 0 K$) for a particular filling by taking the sum of individual states upto the Fermi level (E_F) for both up and down spin electrons. The expression for ground state energy reads,

$$E_0 = \sum_i E_{i,\uparrow} + \sum_i E_{i,\downarrow} + H_0 \quad (4)$$

where, i runs over the states up to the Fermi level. $E_{i,\uparrow}$'s and $E_{i,\downarrow}$'s are the single particle energy eigenvalues ob-

tained by diagonalizing the up and down spin Hamiltonians \mathbf{H}_\uparrow and \mathbf{H}_\downarrow , respectively.

B. Energy band structure

To make this present communication a self contained study let us first start with the energy band structure of a finite width zigzag nano-ribbon.

Non-interacting case: To establish the energy dispersion relation of a zigzag nano-ribbon we find an effective difference equation analogous to the case of an infinite one-dimensional chain. This can be done by proper choice of

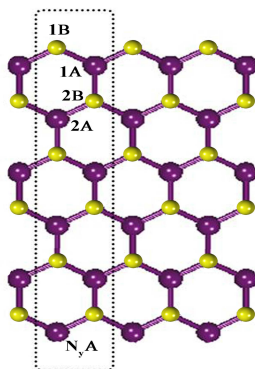


FIG. 4: (Color online). Unit cell configuration of a zigzag nano-ribbon.

a unit cell from the nano-ribbon. The schematic view of the unit cell configuration with N_y pairs of B-A atoms in a zigzag nano-ribbon is shown in Fig. 4. With this arrangement, we express the effective difference equation of the nano-ribbon in the form,

$$(E\mathcal{I} - \mathcal{E}_\sigma)\psi_{j,\sigma} = \mathcal{T}\psi_{j+1,\sigma} + \mathcal{T}^\dagger\psi_{j-1,\sigma} \quad (5)$$

where,

$$\psi_{j,\sigma} = \begin{pmatrix} \psi_{j1B,\sigma} \\ \psi_{j1A,\sigma} \\ \psi_{j2B,\sigma} \\ \vdots \\ \psi_{jN_y A,\sigma} \end{pmatrix}. \quad (6)$$

\mathcal{E} and \mathcal{T} are the site-energy and nearest-neighbor hopping matrices of the unit cell, respectively. \mathcal{I} is a $(2N_y \times 2N_y)$ identity matrix. According to our convention, the translational invariance of the nano-ribbon exists along the x -direction and we can write $\psi_{j,\sigma}$ in terms of the Bloch waves and then Eq. 5 takes the form,

$$(E\mathcal{I} - \mathcal{E}_\sigma) = \mathcal{T}e^{ik_x\Lambda} + \mathcal{T}^\dagger e^{-ik_x\Lambda} \quad (7)$$

where, $\Lambda = \sqrt{3}a$ is the horizontal separation between two filled magenta or yellow circles situated at two successive

unit cells. a is the length of each side of a hexagonal benzene like ring. Finally, we solve Eq. 7 to get the desired energy dispersion relation (E vs. k_x) of the ribbon.

As illustrative example in Fig. 5, we display the variation of energy levels (blue curves) as a function of wave vector k_x for a finite width zigzag nano-ribbon considering $N_y = 4$. At $E = 0$, nearly flat bands appear in the spectrum. The electronic states corresponding to those almost flat bands are strongly localized near the zigzag edges of the tube. The existence of these edge states have also been reported earlier by some other groups^{58,74,75}.

With this energy band structure of a finite width nano-ribbon we now pay attention on the variation of energy levels of a nanotube. In order to get the nanotube from the ribbon we apply periodic boundary condition along the x -direction⁷⁶ which results quantized values of k_x , and the quantized wave numbers are expressed from the

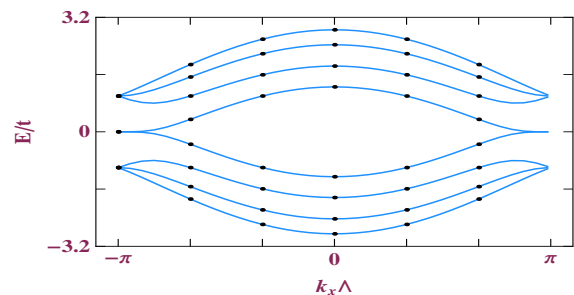


FIG. 5: (Color online). Energy levels (blue curve) as function of k_x for a finite width zigzag nano-ribbon considering $N_y = 4$. The discrete eigenvalues (filled black circles) of a nanotube with $N_x = 12$ and $N_y = 4$, in absence of AB flux ϕ , are superimposed. Here we set $U = 0$.

relation $k_x = 4\pi n_x/N_x\Lambda$, where n_x is an integer lies within the range: $-N_x/4 \leq n_x < N_x/4$. Plugging the quantized values of k_x in Eq. 7 we can easily determine the eigenvalues of a finite sized nanotube. In Fig. 5 we represent the discrete energy eigenvalues (filled black circles) for a zigzag nanotube considering $N_x = 12$ and $N_y = 4$. It is to be noted that the results displayed in Fig. 5 correspond to the case when AB flux ϕ is set equal to zero. With these parameter values of the nanotube k_x gets six quantized values ($-\pi/\Lambda, -2\pi/3\Lambda, -\pi/3\Lambda, 0, \pi/3\Lambda$ and $2\pi/3\Lambda$), and therefore, total 48 energy values are obtained since N_y is fixed at 4.

Interacting case: In the presence of e-e interaction energy levels get modified significantly depending on the filling of electrons. The results calculated for a particular value of U are presented in Fig. 6 where we set $N_y = 4$. In the half-filled band case, a gap opens up at the Fermi energy⁷⁷ which is consistent with the DFT calculations⁷⁸ and the gap increases with the value of U . A careful investigation also predicts that the full energy band gets shifted by the factor $U/2$.

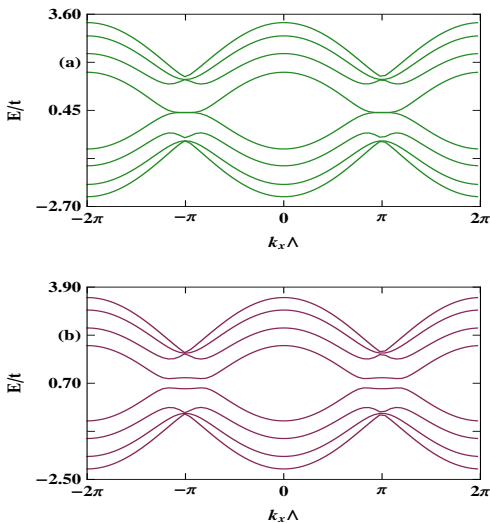


FIG. 6: (Color online). Energy levels as function of k_x for a finite width zigzag nano-ribbon considering $N_y = 4$ and $U = 1.4$, where (a) and (b) correspond to the one-third- and half-filled cases, respectively.

C. Energy-flux characteristics

In this sub-section we examine the energy-flux characteristics of a zigzag nanotube. The results for a zigzag nanotube considering $N_x = 10$ and $N_y = 7$ are displayed in Fig. 7, where (a) and (b) represent $U = 0$ and $U = 1.5$, respectively. In the absence of Hubbard

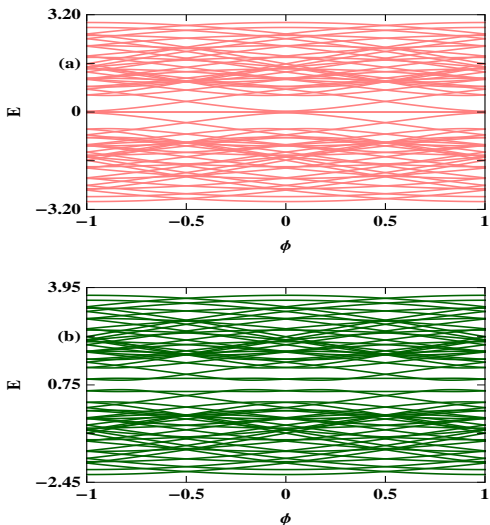


FIG. 7: (Color online). Energy-flux characteristics of a half-filled zigzag nanotube with $N_x = 10$ and $N_y = 7$. (a) $U = 0$ and (b) $U = 1.5$.

interaction ($U = 0$), energy levels are obtained simply by diagonalizing the non-interacting Hamiltonian and the nature of the energy spectrum becomes independent of the total number of electrons N_e in the system. While,

for the interacting case ($U \neq 0$) we employ a mean-field scheme where the interacting Hamiltonian (Eq. 1) are decoupled (for a particular filling) into two non-interacting Hamiltonians corresponding to up and down spin electrons and then diagonalize both \mathbf{H}_\uparrow and \mathbf{H}_\downarrow to get the energy eigenvalues of the system. Since in our case we set $N_x = 10$ and $N_y = 7$, we get total 70 independent energy levels and due to their overlaps individual energy levels are not clearly distinguished from the spectra given in Fig. 7. For identical filling factor of up and down spin electrons the energy levels are exactly similar both for \mathbf{H}_\uparrow and \mathbf{H}_\downarrow (see Fig. 7(b)), and therefore, one energy spectrum cannot be separated from the other. At $E = 0$, the energy levels become almost flat for a wide range of ϕ , and, near $\phi = \pm\phi_0/2$ they vary slowly with ϕ as shown in Fig. 7(a). In Fig. 7(b) the variation of energy levels with ϕ for a zigzag nanotube with the same parameter values stated above are plotted considering Hubbard interaction. Here we choose $U = 1.5$. Both for the up and down spin Hamiltonians the eigenvalues are exactly identical and they overlap with each other. In absence of

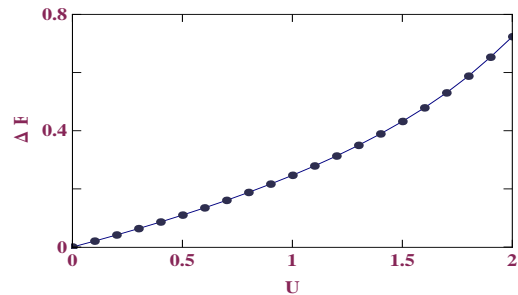


FIG. 8: (Color online). Energy gap (ΔE) as a function of on-site Hubbard interaction strength U for a zigzag nanotube with $N_x = 10$ and $N_y = 7$ in the half-filled band case when ϕ is set at $\phi_0/2$.

interaction there is no gap in the center (around $E = 0$) of the band spectrum (Fig. 7(a)). As soon as the interaction is taken into consideration a finite gap opens up in the band center (Fig. 7(b)) and it increases with the strength of interaction (U) as shown in Fig 8. This energy gap is consistent with the energy gap obtained in the E - k_x diagram (Fig. 6(b)). All these energy levels vary periodically with ϕ providing ϕ_0 ($= 1$ in our chosen unit) flux-quantum periodicity. At half-integer or integer multiples of ϕ_0 , energy levels have either a maximum or a minimum (see Fig. 7). Both the energy spectra take a complicated look as there are many crossings among the energy levels particularly in the regions away from $E = 0$ (Fig. 7).

In Fig. 9 we present the variation of ground state energy of a carbon nanotube with zigzag edges as a function of magnetic flux ϕ for the half-filled band case. Here (a)-(d) represent the four different cases corresponding to four different values of electronic correlation strength $U = 0, 0.5, 1$ and 1.5 , respectively. The energy levels evince one flux-quantum periodicity, as expected, and

their energies get increased with U .

D. Evaluation of persistent current in the second quantized form

Following the second quantized formulation^{79,80}, we estimate persistent current in individual zigzag paths of a nanotube, threaded by an AB flux ϕ . This is an elegant and nice way of studying the response in separate branches of any quantum network.

At first, we express the basic equation of current operator \mathbf{I}_σ corresponding to spin σ in terms of the velocity operator $\mathbf{v}_\sigma (= \dot{\mathbf{x}}_\sigma)$ as,

$$\mathbf{I}_\sigma = -\frac{1}{N_x} e \dot{\mathbf{x}}_\sigma \quad (8)$$

where, \mathbf{x}_σ is the displacement operator. The velocity operator is obtained from the relation,

$$\mathbf{v}_\sigma = \frac{1}{i\hbar} [\mathbf{x}_\sigma, \mathbf{H}_\sigma]. \quad (9)$$

We use this expression to find the velocity operator of an electron with spin σ in a zigzag channel n (say) in the form,

$$\begin{aligned} \mathbf{v}_{n,\sigma} = & \frac{t}{i\hbar} \sum_m \left(\mathbf{b}_{m+1,n,\sigma}^\dagger \mathbf{a}_{m,n,\sigma} e^{-i\theta} \right. \\ & - \mathbf{a}_{m,n,\sigma}^\dagger \mathbf{b}_{m+1,n,\sigma} e^{i\theta} - \mathbf{b}_{m-1,n,\sigma}^\dagger \mathbf{a}_{m,n,\sigma} e^{i\theta} \\ & \left. + \mathbf{a}_{m,n,\sigma}^\dagger \mathbf{b}_{m-1,n,\sigma} e^{-i\theta} \right). \end{aligned} \quad (10)$$

$$\begin{aligned} I_{m-1,m,\sigma}^p = & \frac{it}{2\hbar N_y} \left[\sum_{n=1,3,\dots}^{N_y} (\alpha_{m,n,\sigma}^p \beta_{m-1,n,\sigma}^p e^{-i\theta} - \beta_{m-1,n,\sigma}^p \alpha_{m,n,\sigma}^p e^{i\theta}) + \sum_{n=2,4,\dots}^{N_y} (\beta_{m,n,\sigma}^p \alpha_{m-1,n,\sigma}^p e^{-i\theta} - \alpha_{m-1,n,\sigma}^p \beta_{m,n,\sigma}^p e^{i\theta}) \right. \\ & \left. \times \beta_{m,n,\sigma}^p e^{i\theta} + \beta_{m-1,n,\sigma}^p \alpha_{m-1,n-1,\sigma}^p - \alpha_{m-1,n-1,\sigma}^p \beta_{m-1,n,\sigma}^p \right] + \sum_{n=2,4,\dots}^{N_y-1} (\beta_{m,n+1,\sigma}^p \alpha_{m,n,\sigma}^p - \alpha_{m,n,\sigma}^p \beta_{m,n+1,\sigma}^p) \end{aligned} \quad (14)$$

where, an armchair channel $(m-1, m)$ is constructed by $(m-1)$ -th and m -th lines according to our indexing. It is noteworthy to mention that all the calculations are done at absolute zero temperature ($T = 0K$). Now, the net persistent current driven by electrons of spin σ in a particular channel n for a nanotube described with Fermi energy E_F can be determined by taking the sum of individual contributions from the lowest energy eigenstates up to the Fermi level. Therefore, we have,

$$I_{n,\sigma} = \sum_p I_{n,\sigma}^p. \quad (15)$$

For a particular eigenstate $|\psi_{p,\sigma}\rangle$ persistent current in n -th channel becomes,

$$I_{n,\sigma}^p = -\frac{e}{N_x} \langle \psi_{p,\sigma} | \mathbf{v}_{n,\sigma} | \psi_{p,\sigma} \rangle \quad (11)$$

where, the eigenstate $|\psi_{p,\sigma}\rangle$ is written as,

$$\begin{aligned} |\psi_{p,\sigma}\rangle = & \sum_{m,n} (\alpha_{m,n,\sigma}^p |m, n, \sigma\rangle + \beta_{m-1,n,\sigma}^p |m-1, n, \sigma\rangle \\ & + \beta_{m+1,n,\sigma}^p |m+1, n, \sigma\rangle + \beta_{m,n+1,\sigma}^p |m, n+1, \sigma\rangle), \end{aligned} \quad (12)$$

where, $|m, n, \sigma\rangle$'s are the Wannier states and $\alpha_{m,n,\sigma}^p$ and $\beta_{m,n,\sigma}^p$'s are the corresponding coefficients. Simplifying Eq. 11, we get the final relation of persistent charge current for n -th zigzag channel as,

$$\begin{aligned} I_{n,\sigma}^p = & \frac{iet}{\hbar N_x} \sum_m (\beta_{m+1,n,\sigma}^{p*} \alpha_{m,n,\sigma}^p e^{-i\theta} \\ & - \alpha_{m,n,\sigma}^p \beta_{m+1,n,\sigma}^p e^{i\theta} - \beta_{m-1,n,\sigma}^{p*} \alpha_{m,n,\sigma}^p e^{i\theta} \\ & + \alpha_{m,n,\sigma}^p \beta_{m-1,n,\sigma}^p e^{-i\theta}). \end{aligned} \quad (13)$$

With the above prescription we can also evaluate persistent current in individual armchair paths (along y direction) of the nanotube. Finally, it takes the form,

Taking the contributions from all possible channels n , both up and down spin (σ) electrons, the total persistent current in the nanotube can be expressed as,

$$I_T = \sum_{n,\sigma} I_{n,\sigma}. \quad (16)$$

To judge the accuracy of the persistent current calculated from the present scheme we determine persistent current in some other ways as available in literature. Probably the simplest way of determining persistent current is the case where first order derivative of ground state energy with respect to AB flux ϕ is taken into account^{24,39}.

Therefore, we can write,

$$I_T = -c \frac{\partial E_0(\phi)}{\partial \phi} \quad (17)$$

where, $E_0(\phi)$ is the total ground state energy for a particular electron filling. But, in our present method, the so-called second quantized approach, there are some ad-

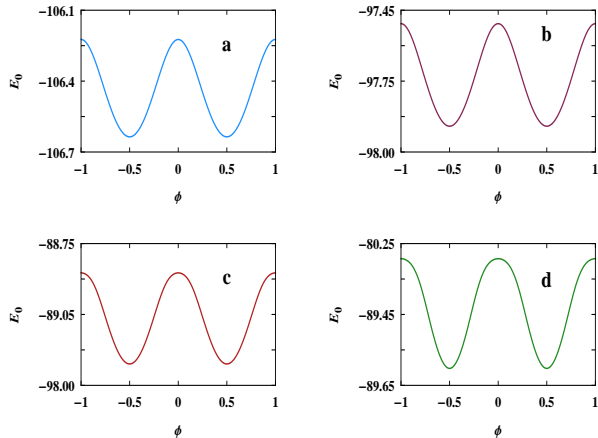


FIG. 9: (Color online). Ground state energy level as a function of ϕ for a zigzag nanotube in the half-filled band case considering $N_x = 20$ and $N_y = 8$. (a), (b), (c) and (d) correspond to $U = 0, 0.5, 1$ and 1.5 , respectively.

vantages compared to other available procedures. With the second quantized formulation we can easily determine current in any branch of a complicated network and the evaluation of individual responses in separate branches helps us to elucidate the actual mechanism of electron transport in a more transparent way.

E. Current-flux characteristics

Now in this subsection we focus our attention on the behavior of persistent current in a zigzag nanotube. Here, also we adopt the unit where $c = h = e = 1$, fix $t = -1$ and measure all the physical quantities in unit of t .

To illustrate the behavior of persistent current in separate branches of a zigzag carbon nanotube we show in Fig. 10 the variation of persistent current in individual zigzag paths as a function of flux ϕ for the half-filled case considering $N_x = 20$ and $N_y = 7$, where (a)-(g) correspond to 1st-7th zigzag channels of the tube, respectively. The Hubbard correlation strength U is fixed at 1.2. Currents carried by up and down spin electrons are displayed in each of these figures simultaneously and they are exactly superposed on each other as the magnitudes and behaviors are exactly similar to each other. All these current profiles exhibit ϕ_0 flux-quantum periodicity. There are no similarity in magnitudes of persistent currents corresponding to separate channels but also another similarity carried by them. Interestingly we

observe that $I_{1\uparrow}$ is exactly identical to $I_{7\uparrow}$, and, similarly for the $(I_{2\uparrow}, I_{6\uparrow})$ and $(I_{3\uparrow}, I_{5\uparrow})$ pairs. $I_{4,\uparrow}$, the current in the middle channel, becomes the isolated one since we have chosen $N_y = 7$. This is true for any zigzag nanotube with odd N_y . For a tube with even N_y , currents are pairwise identical. Summing up the individual currents in seven zigzag channels we get separately the net persistent current carried by up and down spin electrons in the nanotube which is presented in Fig. 10(h) and the total current is obtained by taking both contributions $I_{T\uparrow}$ and $I_{T\downarrow}$ and it is depicted in Fig. 10(i). Now the total current derived from the conventional method where first order derivative of the ground state energy is taken into account, is displayed in Fig. 11. These two net currents calculated from the two different schemes are exactly identical to each other. It emphasizes that the net contribution of persistent current in a zigzag carbon nanotube comes only from the individual zigzag channels, not from the armchair paths. To justify it in Fig. 12 we present the variation of persistent current in an armchair path as a function of ϕ for a half-filled zigzag nanotube considering $N_x = 20$ and $N_y = 7$, which clearly shows zero current for the entire range of ϕ .

In Fig. 7 we have already observed a few almost flat energy levels. These energy levels contribute a very little to the persistent current while, on the other hand, the energy levels with larger slopes provide large persistent current. Also, at the minima or maxima points persistent current becomes zero which is quite obvious since the current is obtained by taking the first order derivative of the eigen energy with respect to flux ϕ (Eq. 17). This peculiar nature of the energy levels invokes the *current amplitude to become filling dependent* and we elaborate it in this section. To clarify this feature in Fig. 13 the current-flux characteristics of a zigzag nanotube, with $N_x = 14$, $N_y = 6$ and $U = 1$, is depicted where four different figures correspond to the four different cases of electron fillings, $N_e = 10, 20, 30$, and 82 . In all these cases, persistent current varies periodically with flux ϕ , exhibiting ϕ_0 flux-quantum periodicity. Also, we observe that there are multiple kinks in the current profiles at different values of ϕ when the number of electrons remains lower than that required for half-filling of the band. These kinks are associated with the multiple crossings of energy levels, as shown in Figs. 13(a)-(c) where the number of electrons are respectively, 10, 20, and 30. This is quite analogous to the feature of persistent current observed in conventional multi-channel mesoscopic cylinders. The behavior of persistent current gets significantly modified when the nanotube becomes half-filled or nearly half-filled. As illustrative example Fig. 13(d) is depicted. As we have already shown a few results for half-filled band case, here we choose $N_e = 82$ i.e., the nanotube is very near to the half-filled band condition. For this choice of parameter values it is examined that all the kinks disappear making the variation of persistent current quite smoother. This is analogous to the behavior of persistent current observed in traditional single-channel mesoscopic rings. For the

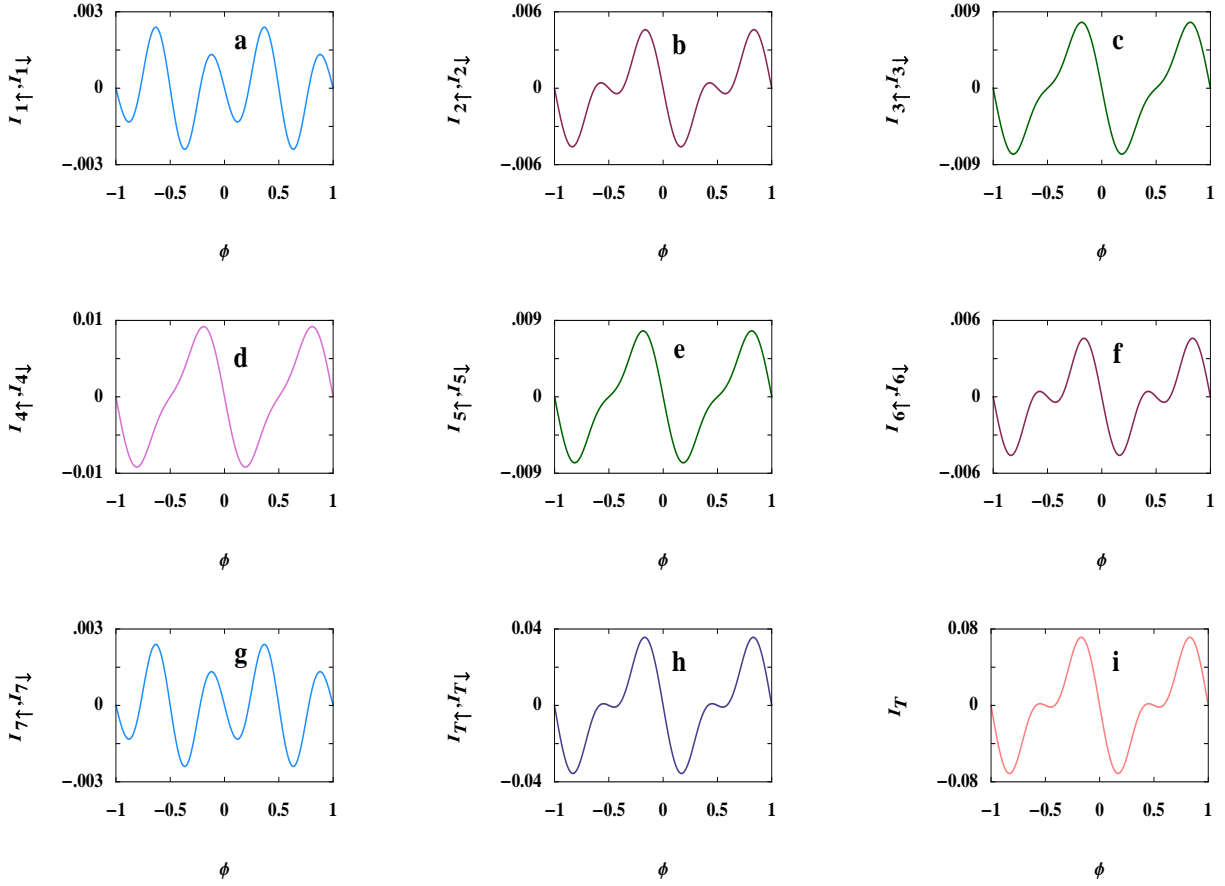


FIG. 10: (Color online). Persistent current in individual zigzag paths as a function of ϕ for a half-filled zigzag nanotube ($N_x = 20$ and $N_y = 7$) with $U = 1.2$, where, (a)-(g) correspond to 1st-7th zigzag channels of the tube, respectively. The net current corresponding to both up and down spin electrons are displayed in (h) while in (i) total persistent current is shown.

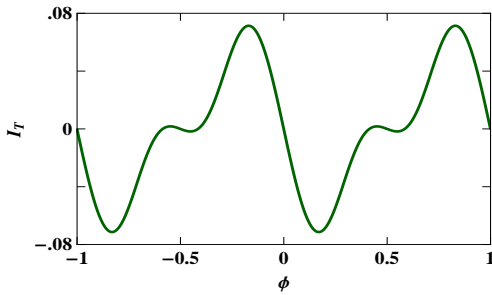


FIG. 11: (Color online). Total persistent current obtained in a traditional derivative approach (Eq. 17) as a function of ϕ for the same parameter values mentioned in Fig. 10.

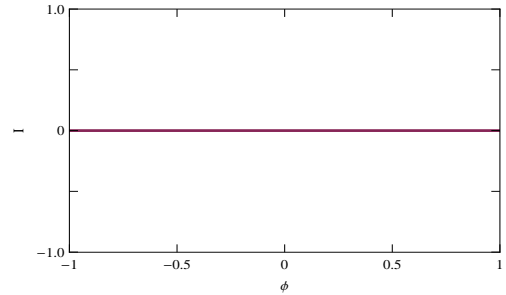


FIG. 12: (Color online). Persistent current in an armchair path as a function of ϕ for a zigzag nanotube with the same parameter values as mentioned in Fig. 10.

cases when the nanotube is far away from half-filling, current amplitudes are quite comparable to each other (see Figs. 13(a)-(c)). On the other hand, when the tube is nearly half-filled current amplitude remarkably gets suppressed and this suppression is very much clear from Fig. 13(d). The reason behind this enormous reduction of current amplitude can be understood clearly when we

look at the E - ϕ characteristics of Fig. 7. At half-filling or very close to half-filling, the top most filled energy level lies in the nearly flat region i.e., around $E = 0$ (see Fig. 7(a)) and it contributes a little to the current. Moreover, when $U \neq 0$, there is gap in the midband region. Now, for a particular filling we find the net persistent current taking the sum of individual contributions from

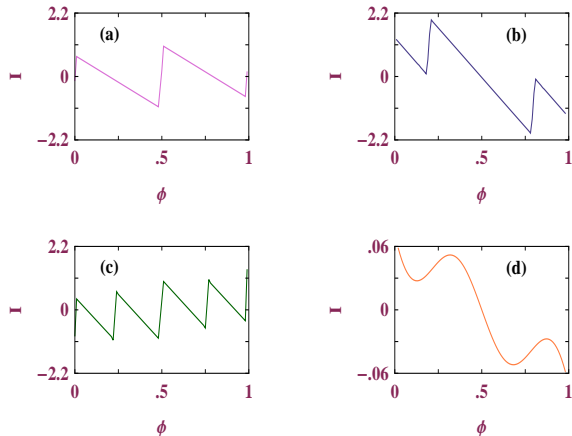


FIG. 13: (Color online). Current-flux characteristics of a zigzag nanotube with $N_x = 14$ and $N_y = 6$, where (a), (b), (c) and (d) correspond to $N_e = 10, 20, 30$ and 82 , respectively. U is fixed at 1.

the lowest filled energy levels, and, in this process only the contribution which comes from the highest occupied energy level finally survives and the rest disappear due to their mutual cancellations. It leads to the enormous reduction of persistent current amplitude in the half-filled or nearly half-filled band case. This feature is independent of the size of the nanotube.

Before we end this section we can emphasize that, the current amplitude in a zigzag nanotube is highly sensitive to the electron filling and this phenomenon can be utilized *in designing a high conducting to a low conducting switching operation and vice versa*.

III. AN ORDERED-DISORDERED SEPARATED NANOTUBE IN PRESENCE OF A MAGNETIC FLUX

This section illustrates the behavior of persistent current in an ordered-disordered separated mesoscopic cylinder. Persistent current in conventional disordered systems have already been reported by many physicists and Anderson type localization⁹ due to disorder is not a new one. But, recent breakthroughs in the growth of semiconductor nanowires have opened up great opportunities to revolutionize technologies in nanoscale electronics⁸¹. Recent experiments on nanowires have already yielded some results in contrast to the phenomenon of strong localization due to doping. For instance, Cui *et al.*⁸² reported that the carrier mobility in boron-doped and phosphorus-doped silicon nanowires under low dopant concentration is extremely low compared to bulk silicon but the conductance becomes diffusive and about five orders of magnitude larger with heavy doping. This motivates us to investigate whether these kinds of shell doped nanowires give rise to new features in the context of persistent current or not.

A. The model

The schematic diagram of the model quantum ordered-disordered separated nanotube is illustrated in Fig. 14, where M co-axial rings are vertically attached and each ring contains N atomic sites. The cylinder is subjected to an AB flux ϕ . For a comparative study we will explore the behavior of persistent currents in a fully disordered and an ordered-disordered separated cylinder simultaneously⁸³. In order to get an ordered-disordered separated

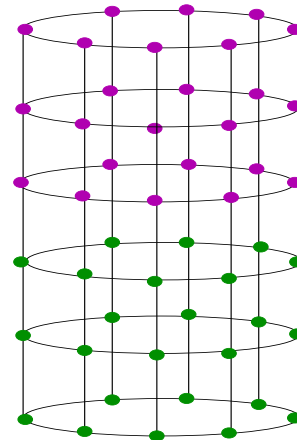


FIG. 14: (Color online). Schematic diagram of a mesoscopic cylinder having 6 rings where each ring contains 8 atomic sites.

cylinder disorders are introduced into $M/2$ number of rings of the lower half of the system (green sites) whereas the remaining part (magenta sites) becomes the ordered one. On the other hand, full disordered system is obtained by putting random disorder in all the atomic sites. A non-interacting single-band tight-binding (TB) Hamiltonian is used to describe the model quantum system which reads as,

$$\begin{aligned} \mathbf{H} = \sum_{m,n} [& \epsilon_{m,n} \mathbf{c}_{m,n}^\dagger \mathbf{c}_{m,n} + t_r (e^{i\theta_r} \mathbf{c}_{m,n}^\dagger \mathbf{c}_{m,n+1} + h.c.) \\ & + t_v (e^{i\theta_v} \mathbf{c}_{m,n}^\dagger \mathbf{c}_{m+1,n} + h.c.)] \end{aligned} \quad (18)$$

where, $\epsilon_{m,n}$ is the on-site energy. For the impurity sites, the site energies $\epsilon_{m,n}$ are selected randomly from a 'Box' distribution function of width $W = 1$. t_r and t_v refer to the intrachannel and interchannel nearest-neighbor couplings, respectively. Here, (m,n) is the co-ordinate of a lattice point where, m and n run from 1 to M and N , respectively. To incorporate the effect of magnetic flux we consider $\theta_r = 2\pi\phi/N$ with the threading magnetic flux ϕ measured in unit of the elementary flux-quantum ϕ_0 . The phase factor along the vertical direction θ_v is taken as zero. $\mathbf{c}_{m,n}^\dagger$ ($\mathbf{c}_{m,n}$) is the creation (annihilation) operator of an electron at the site (m,n) . At absolute zero temperature, the total persistent current of the cylinder is determined from the relation of Eq. 17, where E_0 is the ground state energy of the system which is obtained

by taking the sum over lowest N_e (number of electrons) energy levels.

B. Band structure

In this sub-section we briefly discuss the energy band spectra of a mesoscopic cylinder. To find an analytic form of the energy levels we take a very small sized cylinder having only two rings with 10 sites in each ring. For this smallest possible size of the cylinder, expression of the energy levels takes the form,

$$E = \pm t_v + 2t_r \cos \left[\frac{2\pi(n + \phi)}{N_s \phi_0} \right] \quad (19)$$

where, $N_s (= M \times N)$ is the total number of atomic sites of the cylinder. In Fig. 15 we plot the variation of energy levels as a function of magnetic flux ϕ . The numerical values of the parameters are taken as $t_r = t_v = -1$ and $a = 1$, where a is the lattice parameter. Two energy bands consisting of N number of energy levels within the boundary $E = -1$ to $+3$ and -3 to $+1$ are found to overlap in the region $E = -1$ to $+1$ (in unit of t_r). The width of the overlap region can be tuned by tuning the

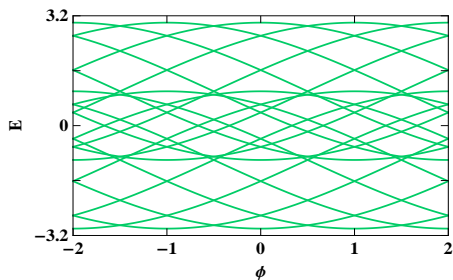


FIG. 15: (Color online). Energy-flux characteristics for a mesoscopic cylinder with 2 rings where each ring contains 10 atomic sites.

vertical hopping strength (t_v). Each energy level exhibits one flux-quantum quantum periodicity. The variation of the energy levels of an ordered multi-channel system are already discussed in the previous section. Effect of the disorder can be attributed to the removal of degeneracy of the energy levels which can be realized from Fig. 16. The results are calculated numerically for a particular disorder configuration. In presence of impurity gap opens up at the crossing points and width of this gap increases with the increase of the disorder strength making the slope of the energy levels smaller and smaller. This makes a remarkable change in magnitude of persistent current. We discuss it in the forthcoming sub-section.

Not only the full disordered cylinder here we also present the energy spectra of an ordered-disordered separated cylinder in Fig. 17, where (a) and (b) correspond to two different values of the disorder strengths, $W = 2.5$ and 5, respectively. Here, the nature of the variation of

energy levels are much more different than that in the case of full disordered system. In order-disordered separated nanotube the energy levels become flatter mainly from the boundary of the spectra.

C. Results and discussion

In order to study the effect of disorder on persistent current in Fig. 18 we plot the typical persistent current amplitude I at a particular value of ϕ as a function of the disorder strength W for an ordered-disordered separated cylinder. Figure (a) corresponds to the results for a half-filled cylinder consisting of 10 rings with 12 sites in each

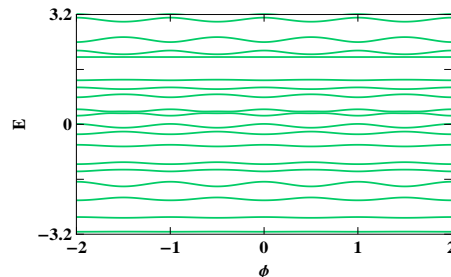


FIG. 16: (Color online). Energy-flux characteristics for a mesoscopic cylinder with the same parameter values mentioned in Fig. 15 in presence of disorder at all atomic sites ($W = 3.5$).

ring and the magnetic flux $\phi = 0.4$. On the other hand, figure (b) represents the results for a half-filled cylinder having 8 rings (10 atomic sites in each ring) in presence of magnetic flux $\phi = 0.2$. Here we compute the root mean square of the current amplitude taking the average over 30 random disordered configurations. We observe that for a full disordered cylinder the current amplitude decreases with the rise of impurity strength W (red curve), while in the case of ordered-disordered separated cylinder the current amplitude initially decreases upto a certain value of W after which it slowly increases with the rise of

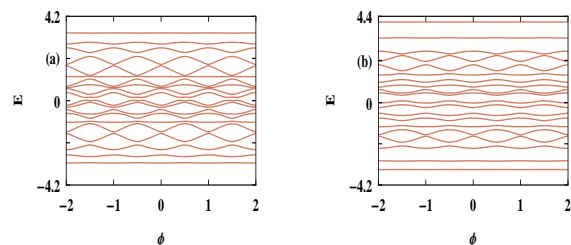


FIG. 17: (Color online). E - ϕ curves for an ordered-disordered mesoscopic cylinder with 2 rings and 10 atomic sites in each ring.

the impurity strength (green curve). This phenomenon can be explained as follows. In the presence of disorder

current amplitude decreases due to the localization of the energy levels which is the so-called Anderson localization. The more impurity strength results the more reduction in current amplitude. This is true only for a full disordered system. But, for the ordered-disordered separated system there is a different physical picture. As we gradually tune the disorder strength towards the higher value, the ordered and disordered regions get decoupled from each other and after a critical limit of W , (say W_c), the cylinder behaves as composed of two completely decoupled regions. At this situation only the ordered region contributes to the current, and thus, the current amplitude gets enhanced with the disorder strength W . The critical value W_c depends on the system size and other

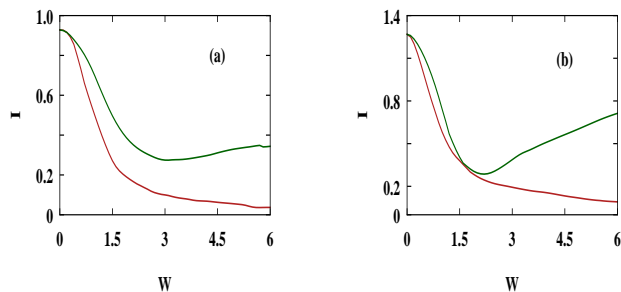


FIG. 18: (Color online). I - W characteristics of an ordered-disordered separated cylinder in the half-filled band case. (a) $M = 10$, $N = 12$ and $\phi = 0.4$ and (b) $M = 8$, $N = 10$, and $\phi = 0.2$. The red and green color correspond to full disordered and half-disordered cylinder.

parameter values like magnetic flux. As for example, it is 3 and 2.5 for two different system sizes as shown in Figs. 18(a) and (b), respectively.

To summarize, in this section we have explored the behavior of persistent current in a disordered and an ordered-disordered separated cylinder in presence a magnetic flux. Most interestingly, we see that the current amplitude shows an anomalous behavior with the increase of impurity strength for an ordered-disordered separated cylinder in contrast to the completely disordered one. This study may be helpful for exploring localization-delocalization transition in shell-doped nanotubes.

IV. A BINARY ALLOY RING WITHOUT EXTERNAL ELECTRODES

In this section we undertake an analysis of the band structure and persistent current in an isolated binary alloy ring (no source and drain electrodes) enclosing a magnetic flux ϕ ⁸⁴

A. The model

Let us concentrate on the simplest model of a binary alloy ring as shown in Fig. 19, where the ring consists of two different types of atoms placed alternately in a regular pattern. They are characterized by two different on-site potential energies, namely, α and β . The ring is subjected to an AB flux ϕ . Within a non-interacting single-band TB framework we illustrate the model of bi-

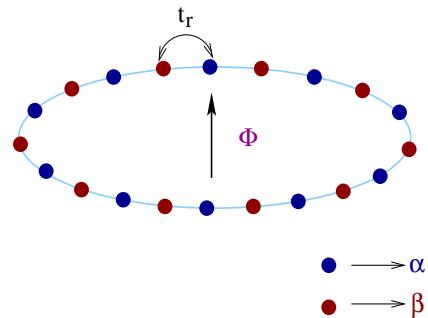


FIG. 19: (Color online). A binary alloy ring, threaded by a magnetic flux ϕ , is composed of two different types of atomic sites, viz, α and β those are represented by filled blue and red circles, respectively.

nary alloy ring and the TB Hamiltonian reads,

$$\mathbf{H}_R = \sum_l (\epsilon_l \mathbf{c}_l^\dagger \mathbf{c}_l + t_r e^{i\theta} \mathbf{c}_l^\dagger \mathbf{c}_{l+1} + t_r e^{-i\theta} \mathbf{c}_{l+1}^\dagger \mathbf{c}_l) \quad (20)$$

where, the on-site energy, ϵ_l takes two values ϵ_α and ϵ_β corresponding to two different sites α and β , respectively. t_r is the nearest-neighbor hopping integral. The phase factor $\theta = 2\pi\phi/N$ of the Hamiltonian takes an account of the effect of the magnetic flux ϕ threaded by the ring which is measured in unit of the elementary flux-quantum ϕ_0 . \mathbf{c}_l^\dagger (\mathbf{c}_l) is the creation (annihilation) operator of an electron at the site l . Here, l runs from 1 to N , where N is the total number of sites in the binary ring.

B. Energy spectrum

Before addressing the main points i.e., the characteristic features of persistent current in an ordered binary alloy ring, let us have an idea about the energy band structure of the system. The analytical expression of energy dispersion relation for the ordered binary alloy ring is as follows,

$$E = \frac{\epsilon_\alpha + \epsilon_\beta}{2} \pm \sqrt{\left(\frac{\epsilon_\alpha - \epsilon_\beta}{2}\right)^2 + 4t_r^2 \cos^2(ka)} \quad (21)$$

where, a is the lattice spacing and k is the wave vector. The periodic boundary condition of the ring sets the quantized values of k in presence of the AB flux ϕ as,

$$k = \frac{2\pi}{Na} \left(n + \frac{\phi}{\phi_0} \right) \quad (22)$$

where, n is an integer and it is restricted within the range: $-N/2 \leq n < N/2$. Throughout our manuscript we consider $\epsilon_\alpha = -\epsilon_\beta = \epsilon$ and Eq. 21 is modified according to this condition as,

$$E = \pm \sqrt{\epsilon^2 + 4t_r^2 \cos^2(ka)}. \quad (23)$$

In Fig. 20 we plot the energy levels as a function of flux ϕ , obtained from Eq. 23, for a 40-site binary alloy ring considering $\epsilon = 1$ and $t_r = 1$. Looking at Fig. 20, two different sets of energy levels are noticed to form two quasi-bands separated by a finite energy gap. This gap, on the other hand, is tunable by the parameter values describing the TB Hamiltonian Eq. 20. The origin of two different sets of energy levels is also clearly understood from Eq. 23. The energy levels of Fig. 20 have either a maximum or a minimum at half-integer or integer multiples of flux-quantum and it results vanishing nature of

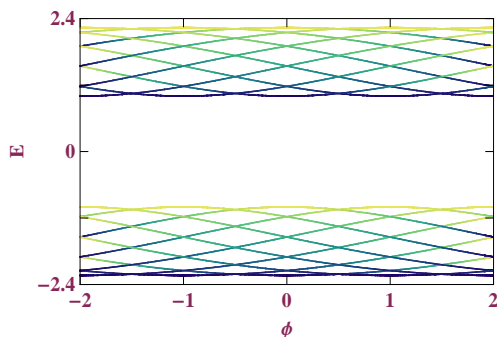


FIG. 20: (Color online). Energy-flux characteristics of an ordered binary alloy ring ($N = 40$) considering $\epsilon_\alpha = -\epsilon_\beta = 1$ and $t_r = 1$. ϕ_0 is set at 1.

persistent current at these specific values of ϕ , since the current is obtained by taking the first order derivative of energy $E(\phi)$ with respect to flux ϕ . All these energy levels vary periodically providing ϕ_0 flux-quantum periodicity, ϕ_0 being 1 in our chosen unit ($c = h = e = 1$).

C. Persistent current

Our task of calculating persistent current for individual energy eigenstates is now easier as we know the energy eigenvalues of the ring as a function of flux ϕ . It is simply the first order derivative of energy with respect to flux ϕ . Therefore, for an n -th energy eigenstate we can write the expression for the current as,

$$I_n = \pm \left(\frac{4\pi t_r^2}{Na\phi_0} \right) \frac{\sin \left[\frac{4\pi}{Na} (n + \phi/\phi_0) \right]}{\sqrt{1 + 4t_r^2 \cos^2 \left[\frac{2\pi}{Na} (n + \phi/\phi_0) \right]}} \quad (24)$$

where, +ve or -ve sign appears in the current expression depending on the choice of n i.e., in which sub-band the energy level exists. To get total persistent current I for a

particular filling N_e , we take the sum of individual contributions from the lowest N_e energy eigenstates as we do our calculations at absolute zero temperature. The expression is,

$$I = \sum_{n=1}^{N_e} I_n \quad (25)$$

Following this way, we plot the variation of persistent current for an ordered 120-site binary alloy ring in Fig. 21. The values of the parameters considered in this figure are

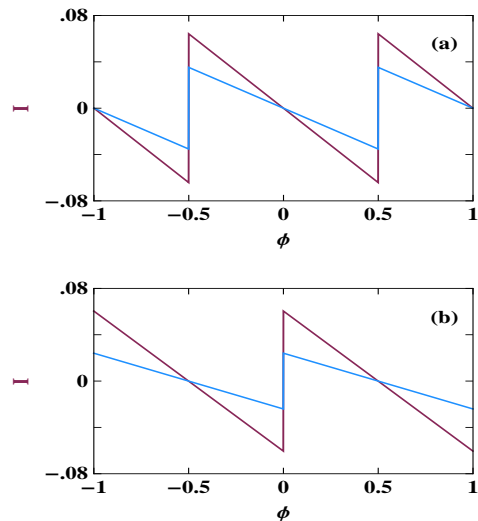


FIG. 21: (Color online). Current-flux characteristics of an ordered binary alloy ring ($N = 120$) considering $\epsilon_\alpha = -\epsilon_\beta = 1$ and $t_r = 1$. The blue and purple colors in (a) correspond to $N_e = 15$ and 35, while in (b) they correspond to $N_e = 10$ and 30, respectively. The lattice spacing a is set at 1 and we choose $\phi_0 = 1$.

$\epsilon = 1$ and $t_r = 1$. In both figures, Fig. 21(a) and (b), the current profiles show saw-tooth like variation as a function of flux ϕ , similar to that of traditional single-channel mesoscopic rings⁸⁵. The purple and blue colors correspond to two different fillings of the band. For odd number of electrons the results are shown in Fig. 21(a) while, in Fig. 21(b) the results are given for even number of electrons. The sharp transitions at half-integer (for odd N_e) or integer (for even N_e) multiples of flux-quantum (ϕ_0) in persistent current appears due to the crossing of energy levels at these respective values of ϕ . Quite interestingly, we also examine that the current shows always diamagnetic response irrespective of the filling factor.

V. A BINARY ALLOY RING WITH EXTERNAL ELECTRODES

Upto now we have discussed the basic features of persistent current in different isolated mesoscopic systems. In this section we extend our analysis of persistent current to an open system where a binary alloy ring⁸³ is

clamped between two semi-infinite one-dimensional (1D) electrodes. The behavior of persistent current in presence of transport current will also be analyzed.

A. The model

Let us start by referring to Fig. 22 where a binary alloy ring, threaded by a magnetic flux ϕ , is attached to two semi-infinite one-dimensional metallic electrodes, namely, left-lead and right-lead, via two atomic sites labeled as μ and ν . The total numbers of identical pairs of α - β sites in the binary ring is N_1 . Now we incorporate some foreign atoms denoted by γ having on-site potentials ϵ_γ in any one of the two arms of the ring. Here, we choose the upper arm in this purpose. There are N_2 identical foreign atomic sites, embedded together in a small

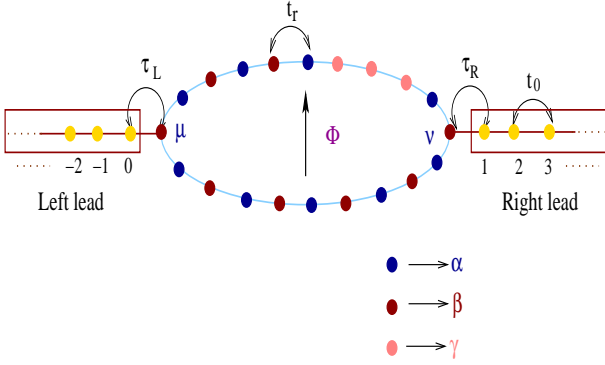


FIG. 22: (Color online). A binary alloy ring in presence of some identical foreign atoms (labeled as γ sites), threaded by an AB flux ϕ , is attached to two semi-infinite one-dimensional metallic leads. μ and ν are the connecting sites.

portion of the ring. These γ sites are often referred to as impurity sites in the present manuscript. We enumerate the atomic sites of the two side-attached leads in a particular way, as shown in Fig. 22. A single-band non-interacting TB framework is used to describe the entire system. For the full system we can partition the total Hamiltonian as a sum of three terms like,

$$\mathbf{H} = \mathbf{H}_R + \mathbf{H}_L + \mathbf{H}_T \quad (26)$$

where, \mathbf{H}_R , \mathbf{H}_L and \mathbf{H}_T represent the Hamiltonians for the ring, leads (left and right) and coupling between the ring and leads, respectively. The ring Hamiltonian (\mathbf{H}_R) takes the form exactly similar to Eq. 20, but instead of two possible on-site potentials here ϵ_l has three possibilities for three different atomic sites (α , β and γ). By means of some external gate voltage V_g , the site energy ϵ_γ can be tuned and accordingly the site-energies are changed. Thus we express the on-site energy of a single γ atom like, $\epsilon_\gamma = \epsilon_\gamma^0 + V_g$, where ϵ_γ^0 is the site energy in absence of any external potential. The other two terms of Eq. 26, \mathbf{H}_L and \mathbf{H}_T , can also be written in a similar

fashion as,

$$\mathbf{H}_L = t_0 \underbrace{\sum_{m \leq 0} (\mathbf{b}_m^\dagger \mathbf{b}_{m-1} + h.c.)}_{\text{left lead}} + t_0 \underbrace{\sum_{m \geq 1} (\mathbf{b}_m^\dagger \mathbf{b}_{m+1} + h.c.)}_{\text{right lead}} \quad (27)$$

and,

$$\mathbf{H}_T = (\tau_L \mathbf{b}_0^\dagger \mathbf{c}_\mu + \tau_R \mathbf{b}_1^\dagger \mathbf{c}_\nu) + h.c. \quad (28)$$

where \mathbf{b}_m^\dagger (\mathbf{b}_m) are the creation (annihilation) operator of an electron at the site m of the leads and t_0 represents the nearest-neighbor hopping strength within these leads. We set the site energy for the identical sites in the leads to zero and due to this reason in Eq. 27 we have omitted the site-energy terms. Here, τ_L is the coupling strength between the left lead and the ring, while it is τ_R for the other case.

B. Wave-guide theory

To find transmission probability across the ring and also to calculate persistent current in such an open ring geometry we adopt the wave-guide theory^{45,49}. In the present sub-section we describe the formulation very briefly.

We begin with the Schrödinger equation $H|\psi\rangle = E|\psi\rangle$, where $|\psi\rangle$ is the stationary wave function of the entire system. In the Wannier basis it ($|\psi\rangle$) can be expressed as,

$$|\psi\rangle = \underbrace{\sum_{m \leq 0} B_m |m\rangle}_{\text{left lead}} + \underbrace{\sum_{m \geq 1} B_m |m\rangle}_{\text{right lead}} + \underbrace{\sum_l C_l |l\rangle}_{\text{ring}} \quad (29)$$

where, the co-efficients B_m and C_l correspond to the probability amplitudes in the respective sites. Keeping in mind the periodicity of the ordered binary ring we write the wave functions associated with the electrons as a plane wave and the wave amplitudes in the left and right leads are,

$$B_m = e^{ikm} + r e^{-ikm}, \quad \text{for } m \leq 0 \quad (30)$$

and

$$B_m = t e^{ikm}, \quad \text{for } m \geq 1 \quad (31)$$

where, r and t are the reflection and transmission amplitudes, respectively. k is the wave number and it is related to the energy E of the incident electron by the expression $E = 2t_0 \cos k$. The lattice spacing a is set equal to 1.

In order to find out the transmission amplitude t , we have to solve the following set of coupled linear equations.

$$\begin{aligned} EB_0 &= t_0 B_{-1} + \tau_L C_\mu \\ (E - \epsilon_l) C_l &= t_r e^{i\phi} C_{l+1} + t_r e^{-i\phi} C_{l-1} + \tau_L B_0 \delta_{l,\mu} \\ &\quad + \tau_R B_1 \delta_{l,\nu} \\ EB_1 &= t_0 B_2 + \tau_R C_\nu \end{aligned} \quad (32)$$

where, the co-efficients B_0 , B_{-1} , B_1 and B_2 can be easily expressed in terms of r and t by using Eqs. 30 and 31, and they are in the form:

$$\begin{aligned} B_0 &= 1 + r \\ B_{-1} &= B_0 e^{ik} - 2i \sin k \\ B_1 &= t e^{ik} \\ B_2 &= t e^{2ik} \end{aligned} \quad (33)$$

Thus, for a particular value of E we can easily solve the set of linear equations and find the value of t . Finally, the transmission probability across the ring becomes

$$T(E) = |t|^2. \quad (34)$$

Now, to compute the persistent current between any two neighboring sites in the binary ring we use the following relation,

$$I_{l,l+1} = \frac{2et_r}{N\hbar} \text{Im} \left(C_l^\dagger C_{l+1} e^{-i\phi} \right). \quad (35)$$

C. Transmission and average density of states

Throughout our calculations we set $\epsilon = 1$, $\epsilon_\gamma^0 = 0$, $t_r = 1$, $\epsilon_0 = 0$ and $t_0 = 2$. The energy scale is measured in unit of t_r .

Two-terminal transmission probability T (orange color) as a function of injecting electron energy E for some typical binary alloy rings considering different number of impurity sites is displayed in Fig. 23 where (a), (b) and (c) correspond to three different numbers of impurity atoms. Figure (a) represents the transmission spectrum of the binary alloy ring with 28 pairs of α - β atoms but without any foreign impurity atoms while (b) and (c) correspond to $N_2 = 12$ and 22, respectively, keeping N_1 fixed to 28. The average density of states (ADOS) is also superimposed in each spectrum. In all these cases the magnetic flux ϕ is set equal to zero. The results are quite interesting. In absence of any impurity site the transmission spectrum is characterized by two bands separated by a finite gap and the gap between these two bands are also tunable by the parameter values describing the system. Looking back at Fig. 20 the band splitting for the ordered binary alloy ring is easily understood and we predict that the spectrum is just the finger print of the system energy levels. This transmission spectrum exactly overlaps with the ADOS profile (ρ - E spectrum) which ensures that electronic transmission takes place through all the energy eigenstates of the binary alloy ring and they are extended in nature. The situation becomes really interesting when some additional impurities (γ sites) are introduced in any part of the binary alloy ring. Due to the inclusion of such atomic sites some energy levels appear within the band of extended regions those are no longer extended, but they are almost quasi-localized and do not contribute to the electronic transmission. This

behavior is elaborated in Figs. 23(b) and (c), where T - E and ρ - E spectra are superimposed with each other for two different numbers of impurity sites (N_2). In the band center, several energy levels appear and these levels do not provide any contribution to the transmission of electrons. They are almost localized in nature. Mainly the states within the two bands are responsible for electron transmissions. The number of the almost localized energy levels increases with the increase of the number of the impurity sites, and for sufficiently large number of impurities they form a quasi-energy band of localized

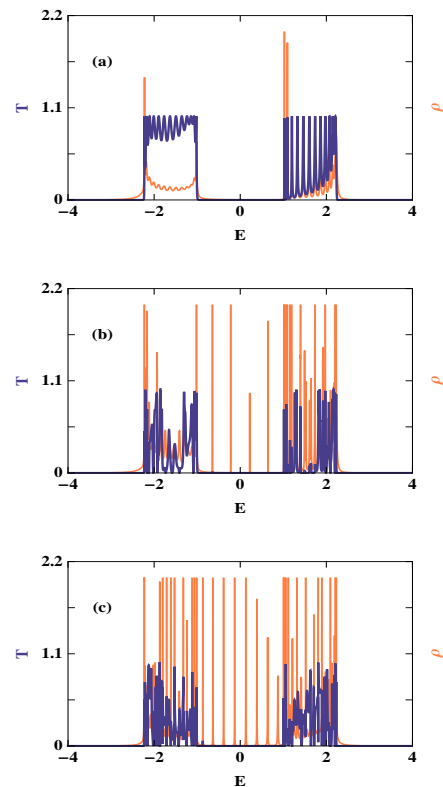


FIG. 23: (Color online). Transmission probability (orange color) and average density of states (dark-blue color) for some typical binary alloy rings with fixed number of α - β pairs ($N_1 = 28$), but different values of impurity sites N_2 , where (a) $N_2 = 0$, (b) $N_2 = 12$ and (c) $N_2 = 22$. For these three cases we set $\mu = 1$ and choose $\nu = 29, 35$ and 40 , respectively. Other parameters are: $\epsilon_\gamma = 0$, $\tau_L = \tau_R = 1$ and $\phi = 0$.

states. The location of the localized energy band can be shifted towards the edge of extended regions simply by tuning the site energy of these foreign atoms, and this can be done by means of applying an external gate voltage V_g . We utilize this feature to make the binary alloy ring behave like an extrinsic semiconductor, either p -type or n -type by tuning the Fermi level to an appropriate place.

We plot Fig. 24 to explore the semiconductor-like behavior of the binary ring. The variation of transmission probability and the ADOS are shown in this figure. Here, we consider a binary ring with 60 identical pairs of α - β

sites and 44 number of impurity sites. Two different cases are exhibited in Fig. 24(a) and (b) for two different values of the on-site potential energies of the γ atoms. Figure (a) represents the transmission spectrum of the binary alloy ring when ϵ_γ is set at 0.6 while the other figure (Fig. 24(b)) corresponds to $\epsilon_\gamma = -0.6$. In presence of the impurity atoms we get almost quasi-energy bands (ADOS spectra) and quite interestingly we observe that when ϵ_γ is fixed at 0.6, a localized energy band for a wide range of energy is formed along the left edge of the extended region (Fig. 24(a)). Now, if the Fermi level is set around $E = -1.7$, then many electrons in the localized region below the Fermi level can jump easily, even at much low temperature since the energy gap is almost zero, to the extended regions and can contribute to the current. As a

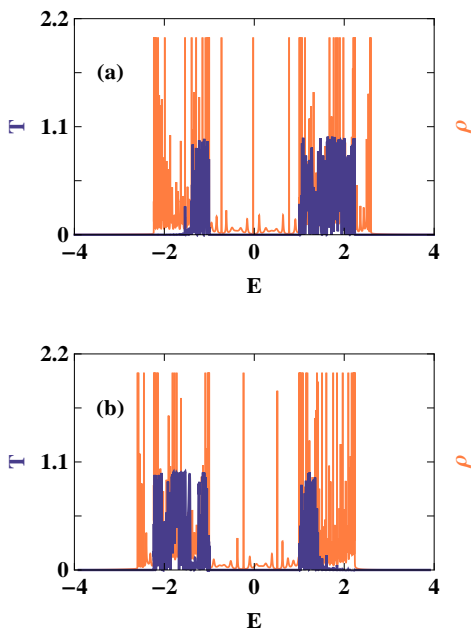


FIG. 24: (Color online). Transmission probability (orange color) and ADOS (dark-blue color) as a function of energy for a binary alloy ring ($N_1 = 60$) with 44 impurity sites ($N_2 = 44$), where (a) and (b) correspond to $\epsilon_\gamma = 0.6$ and -0.6 , respectively. Other parameters are: $\phi = 0$, $\tau_L = \tau_R = 1.5$, $\mu = 1$ and $\nu = 83$.

result large number of excess electrons become available in the conduction band region which behave as n-type carriers. This movement however depends on the localized energy levels and also the available extended energy states. On the contrary, when the site-energies of the γ atoms are tuned to another value, say, -0.6 an exactly opposite behavior is obtained. In this case the wide band of localized states is formed in the right edge of the extended region (see Fig. 24(b)). Now, if the Fermi level is tuned to appropriate place, around $E = 1.7$ in this case, then the electrons from the filled extended levels below the Fermi level hop to the nearly empty localized levels, and these electrons do not contribute anything to

the current. But, the absence of electrons are realized by holes in the extended regions which can carry current and the system behaves like a p -type carriers. Before we end this discussion, we can emphasize that by setting the Fermi level in appropriate places our model quantum system can be tailor-made to use as a p -type or an n -type semiconductor.

At the end of this sub-section we would like to mention a few points. To establish the fact that how such a geometry can be utilized as a p -type or an n -type semiconductor with appropriate choice of the Fermi level we have taken a particular set of parameter values. As we are doing a model calculation it is very easy to take some specific values of the parameters and use in our numerical calculations, but all these physical phenomena are exactly invariant with the change of the parameter values. Only the numerical values will be altered. These features are also exactly valid even for a non-zero value of magnetic flux ϕ . The physical picture will be much more appealing

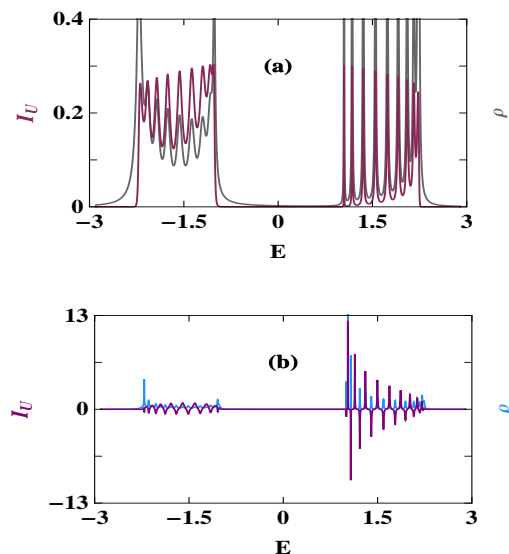


FIG. 25: (Color online). Persistent current (I_U) in the upper arm (red and violet color) as a function of energy E for a binary alloy ring ($N_1 = 20$) in the absence of impurity atoms ($N_2 = 0$), where (a) $\phi = 0$ and (b) $\phi = \phi_0/4$. Other parameters are: $\tau_L = \tau_R = 0.8$, $\mu = 1$ and $\nu = 21$. For this ordered ring, persistent current in the lower arm (I_L) is exactly identical to I_U . ADOS profile (gray and light-blue color) is also superimposed in each spectrum.

if we consider larger rings with more impurity sites and it gives us the confidence to propose an experiment in this way. In a recent work Bellucci *et al.*^{86,87} have done a detailed study of magneto-transport properties in quantum rings considering tunnel barriers in the presence of magnetic field and shown how metal-to-insulator transition takes place in such a geometry. They have also established that by controlling the strength and the positions of the barriers, the energy shift can be done in a tunable way. This is quite analogous to our present study, and

so, an experiment in this regard will be challenging.

D. Persistent current in presence of transport current

Now we focus on the characteristic features of persistent current in the binary alloy ring in presence of external bias voltage. We also study the role of magnetic field in this context. In Fig. 25 upper arm current, I_U , in the upper arm of an ordered binary alloy ring as a function of energy E is presented where (a) and (b) correspond to $\phi = 0$ and $\phi_0/4$, respectively. Due to conservation of current at the junction points, current between any two sites are equal to each other. We refer upper arm current to the bond current between any two nearest-neighbor atomic sites of the upper arm. The ring is symmetrically coupled to the side attached leads i.e., the upper and lower arms have identical length, and accordingly, the current I_L in the lower arm becomes exactly identical to

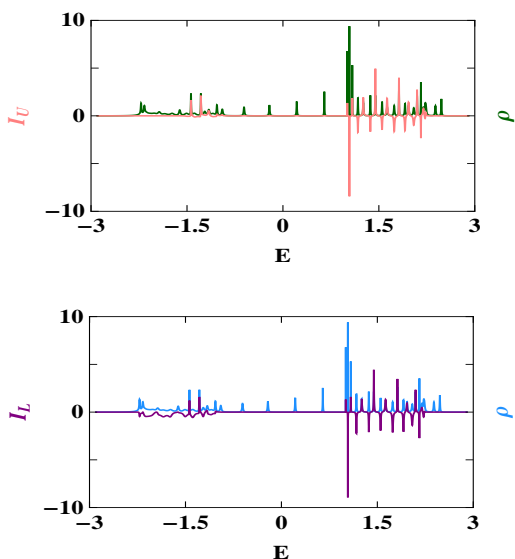


FIG. 26: (Color online). Persistent current as a function of energy for a binary alloy ring ($N_1 = 16$) in presence of impurity sites ($N_2 = 12$) for a finite value of ϕ ($\phi = 0.3$), where (a) and (b) correspond to the currents for the upper (pink color) and lower (violet color) arms respectively. Other parameters are: $\epsilon_\gamma = 0.5$, $\tau_L = \tau_R = 0.8$, $\mu = 1$ and $\nu = 23$. ADOS profile (green and light-blue color) is superimposed in each spectrum.

the current obtained in the upper arm. Similarly, we define the lower arm current. Here, again the band-splitting put its mark on the current density profile. Finite current is available for two wide range of energies, separated by a finite gap, associated with the energy levels of the ring those are clearly visible from the ADOS profiles (green and light-blue color). The quite exact superposition of the current profile and the AVDOS profile invokes the extended natures of all these energy eigenstates in our

mind. Additionally, all the values of the current are positive i.e. they are in the same phase ensuring the fact that this current is completely due the transport current between the two leads fixed at two different chemical potentials as there is only one driving force, the external bias. This phenomenon depicted in Fig. 25(a) correspond to zero magnetic flux. As well as the magnetic field with flux density ϕ is switched on, not only both the positive and negative values of current appear indicating opposite phases but also they appear in regular alternative fashion as shown in Fig. 25(b). Moreover, the magnitudes are also different in these two cases indicating the effect quantum interference of mesoscopic regime. Therefore, by measuring persistent current we can directly estimate the nature of the current i.e., whether it is paramagnetic

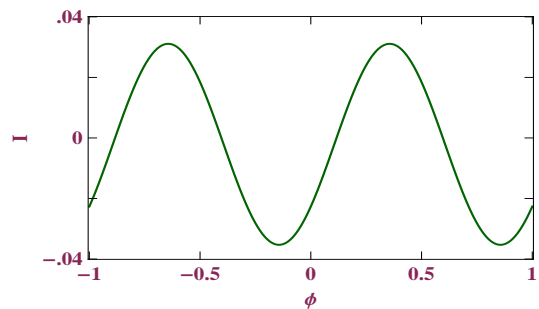


FIG. 27: (Color online). Persistent current as a function of magnetic flux for a binary alloy ring ($N_1 = 16$) in presence of impurity sites ($N_2 = 12$) with $V_g = 0.5$ Other parameters are: $\tau_L = \tau_R = 0.8$, $\mu = 1$ and $\nu = 23$.

or diamagnetic in nature and also predict the characteristics of energy eigenstates, which are somewhat interesting in the study of electron transport. Needless to say, magnetic field plays an important role in this context.

Already stated in introduction the current can persists in this kind of loop geometry if we set the lengths of two arms unequal or put any kind of static disorder in path of the electron or in any other way we can disturb the wave function or create any path difference between the wave functions corresponding to different arms. In our study we incorporate impurities in the upper arm of the binary ring as mentioned earlier. The results are displayed in Fig. 26 where (a) and (b) represent the cases corresponding to the upper and lower arms of the ring, respectively. To plot the curve we consider a typical binary alloy ring with $N_1 = 16$ and $N_2 = 12$. With the inclusion of impurity sites, the symmetry between the two arms is broken, and therefore, the currents in the upper and lower arms are no longer identical to each other as shown from the spectra (Figs. 26(a) and (b)). So, there must be a circulating current within the ring which is the so-called persistent current in presence of transport current. Unlike to the ordered binary alloy ring (Fig. 25), here all the energy eigenstates are not extended in nature. Some localized energy levels appear in the band of extended energy states due to the presence

of impurity sites in the ring. This is clearly visible from the spectra since for these impurity levels no current is available. We also check the periodicity of the persistent current. It is shown in Fig. 27. Persistent current exhibits ϕ_0 flux-quantum periodicity. Thus, calculating persistent current we can emphasize the nature of energy eigenstates very nicely, and this idea can be utilized to reveal the localization properties of energy eigenstates in any complicated geometry.

VI. CONCLUDING REMARKS

To conclude, in the present article we have made a detailed investigation of magneto-transport in both closed and open mesoscopic systems. We have started with the discussion of a zigzag nanotube pierced by a magnetic flux using a generalized Hartree-Fock mean field approach. Based on the tight-binding model we explore the effect of the Hubbard interaction on the energy levels of the tube. After describing different numerical results we have established the second quantized form to evaluate persistent current in individual paths of a zigzag carbon nanotube and based on this formulation we have also presented the numerical results for the distribution of persistent current in different branches of the nanotube. From the current-flux characteristics we have emphasized that the current amplitude in the zigzag nanotube is highly sensitive to the electron filling and this phenomenon can be utilized in designing a high conducting to a low conducting switching device and vice versa. Following the

study of nanotube we have explored the persistent current in an ordered-disordered separated cylinder penetrated by a magnetic flux. Most interestingly, we have seen that the current amplitude shows an anomalous behavior with the increase of impurity strength. This study may be helpful for exploring localization-delocalization transition in shell-doped nanotubes. To discuss persistent current in open system i.e., system with side-attached electrodes we have considered a binary alloy ring in presence of a magnetic flux ϕ , as an illustrative example. Within a single-band non-interacting TB framework persistent current and band structure of an isolated ordered binary alloy ring have been analyzed. Then, we have explored the magneto-transport properties of a binary alloy ring in presence of external electrodes. The effect of impurities have also been addressed. Quite interestingly we have noticed that in the presence of some foreign atoms, those are not necessarily be random, in any part of the ring, some quasi-localized energy levels appear within the band of extended energy levels. The locations of these almost localized energy levels can also be regulated by means of some external gate voltage. This leads to a possibility of using such a system as a p -type or an n -type semiconductor by fixing the Fermi level in appropriate places.

Before we end, we would like to mention that in the present review we have addressed some important aspects of quantum transport through some low-dimensional model quantum systems. Several other important quantum phenomena in such meso- and nano-scale systems have also been reported in recent reviews^{88–93}.

-
- * Electronic address: paramita.dutta@saha.ac.in
 † Electronic address: santanu.maiti@isical.ac.in
- ¹ S. Datta, *Electronic transport in mesoscopic systems*, Cambridge University Press, Cambridge (1997).
 - ² P. Singha Deo and A. M. Jayannavar, Phys. Rev. B **50**, 11629 (1994).
 - ³ *Quantum coherence in mesoscopic systems*, NATO Advanced Study Institute Series B: Physics **254**, ed. by B. Kramer, Plenum, New York (1991).
 - ⁴ *Mesoscopic phenomenon in solids*, ed. by B. L. Altshular, P. A. Lee, and R. A. Webb, Noth-Holland (1991).
 - ⁵ C. W. J. Beenakker and H. van Houten, *Solid state physics: Semiconductor heterostructures and nanostructures* **44**, ed. by H. Ehrenreich and D. Turnbull, Academic Press (1991).
 - ⁶ S. Washburn and R. A. Webb, Adv. Phys. **35**, 375 (1986).
 - ⁷ N. Kumar and A. M. Jayannavar, Phys. Rev. B **32**, 3345 (1985).
 - ⁸ P. Singha Deo and A. M. Jayannavar, Mod. Phys. Lett. B **7**, 1045 (1993).
 - ⁹ P. W. Anderson, Phys. Rev. **109**, 1492 (1958).
 - ¹⁰ K. v. Klitzing, G. Dorda, and M. Pepper, Phys. Rev. Lett. **45**, 494 (1980).
 - ¹¹ Y. Aharonov and D. Bohm, Phys. Rev. **115**, 485 (1959).
 - ¹² A. van Oudenaarden, M. H. Devoret, Y. V. Nazarov, and J. E. Mooij, Nature **391**, 768 (1998).
 - ¹³ O. Hod, E. Rabani, and R Baer, Acc. Chem. Res. **39**, 109 (2006).
 - ¹⁴ F. Nichele, Y. Komijani, S. Hennel, C. Gerl, W. Wegscheider, D. Reuter, A. D. Wieck, T. Ihn, and K. Ensslin, New J. Phys. **15**, 033029 (2013).
 - ¹⁵ N. Bayers and C. N. Yang, Phys. Rev. Lett. **7**, 46 (1961).
 - ¹⁶ M. Büttiker, Y. Imry, and R. Landauer, Phys. Lett. A **96**, 365 (1983).
 - ¹⁷ L. P. Levy, G. Dolan, J. Dunsmuir, and H. Bouchiat, Phys. Rev. Lett. **64**, 2074 (1990).
 - ¹⁸ R. Deblock, R. Bel, B. Reulet, H. Bouchiat, and D. Mailly, Phys. Rev. Lett. **89**, 206803 (2002).
 - ¹⁹ B. Reulet, M. Ramin, H. Bouchiat, and D. Mailly, Phys. Rev. Lett. **75**, 124 (1995).
 - ²⁰ H. F. Cheung, Y. Gefen, E. K. Reidel, and W. H. Shih, Phys. Rev. B **37**, 6050 (1988).
 - ²¹ V. Ambegaokar and U. Eckern, Phys. Rev. Lett. **65**, 381 (1990).
 - ²² A. Schmid, Phys. Rev. Lett. **66**, 80 (1991).
 - ²³ U. Eckern and A. Schmid, Europhys. Lett. **18**, 457 (1992).
 - ²⁴ S. K. Maiti, Solid State Commun. **150**, 2212 (2010).
 - ²⁵ S. K. Maiti, M. Dey, S. Sil, A. Chakrabarti, and S. N. Karmakar, Europhys. Lett. **95**, 57008 (2011).
 - ²⁶ S. K. Maiti, J. Chowdhury, and S. N. Karmakar, Phys. Lett. A **332**, 497 (2004).

- ²⁷ S. K. Maiti, J. Chowdhury, and S. N. Karmakar, *Solid State Commun.* **135**, 278 (2005).
- ²⁸ S. K. Maiti, *J. Appl. Phys.* **110**, 064306 (2011).
- ²⁹ S. K. Maiti, *Phys. Status Solidi B* **248**, 1933 (2011).
- ³⁰ D. Mailly, C. Chapelier, and A. Benoit, *Phys. Rev. Lett.* **70**, 2020 (1993).
- ³¹ E. M. Q. Jariwala, P. Mohanty, M. B. Ketchen, and R. A. Webb, *Phys. Rev. Lett.* **86**, 1594 (2001).
- ³² R. Deblock, R. Bel, B. Reulet, H. Bouchiat, and D. Mailly, *Phys. Rev. Lett.* **89**, 206803 (2002).
- ³³ H. Bluhm, N. C. Koshnick, J. A. Bert, M. E. Huber, and K. A. Moler, *Phys. Rev. Lett.* **102**, 136802 (2009).
- ³⁴ W. Rabaud, L. Saminadayar, D. Mailly, K. Hasselbach, A. Benoit, and B. Etienne, *Phys. Rev. Lett.* **86**, 3124 (2001).
- ³⁵ V. Chandrasekhar, R. A. Webb, M. J. Brady, M. B. Ketchen, W. J. Gallagher, and A. Kleinsasser, *Phys. Rev. Lett.* **67**, 3578 (1991).
- ³⁶ M. Abraham and R. Berkovits, *Phys. Rev. Lett.* **70**, 1509 (1993).
- ³⁷ G. Bouzerar, D. Poilblanc, and G. Montambaux, *Phys. Rev. B* **49**, 8258 (1994).
- ³⁸ T. Giamarchi and B. S. Shastry, *Phys. Rev. B* **51**, 10915 (1995).
- ³⁹ S. K. Maiti, J. Chowdhury, and S. N. Karmakar, *J. Phys.: Condens. Matter* **18**, 5349 (2006).
- ⁴⁰ H. F. Cheung, Y. Gefen, E. K. Reidel, and W. H. Shih, *Phys. Rev. B* **37**, 6050 (1988).
- ⁴¹ O. Entin-Wohlman and Y. Gefen, *Europhys. Lett.* **8**, 477 (1989).
- ⁴² H. Bary-Soroker, O. Entin-Wohlman, and Y. Imry, *Phys. Rev. B* **82**, 144202 (2010).
- ⁴³ M. Büttiker, *Phys. Rev. B* **32**, R1846 (1985).
- ⁴⁴ E. Akkermans, A. Auerbach, J. E. Avron, and B. Shapiro, *Phys. Rev. Lett.* **66**, 76 (1991).
- ⁴⁵ J. -B. Xia, *Phys. Rev. B* **45**, 3593 (1992).
- ⁴⁶ P. A. Mello, *Phys. Rev. B* **47**, 16358 (1993).
- ⁴⁷ P. A. Orellana, M. L. Ladrón de Guevara, M. Pacheco, and A. Latgé, *Phys. Rev. B* **68**, 195321 (2003).
- ⁴⁸ A. M. Jayannavar and P. Singha Deo, *Phys. Rev. B* **49**, 13685 (1994).
- ⁴⁹ Y. -J. Xiong and X. -T. Liang, *Phys. Lett. A* **330**, 307 (2004).
- ⁵⁰ T. P. Pareek, P. Singha Deo, and A. M. Jayannavar, *Phys. Rev. B* **52**, 14657 (1995).
- ⁵¹ S. Bellucci and P. Onorato, *Physica E* **41**, 1393 (2009).
- ⁵² P. Singha Deo and A. M. Jayannavar, *Phys. Rev. B* **51**, 10175 (1995).
- ⁵³ A. M. Jayannavar, P. Singha Deo, and T. P. Pareek, *Physica B* **212**, 261 (1995).
- ⁵⁴ P. Singha Deo and A. M. Jayannavar, *Mod. Phys. Lett. B* **7**, 1045 (1993).
- ⁵⁵ P. Dutta, S. K. Maiti, and S. N. Karmakar, arXiv:1307.2103v2.
- ⁵⁶ O. O. Kit, T. Talliner, L. Mahadevan, J. Timonen, and P. Koskinen, *Phys. Rev. B* **85**, 085428 (2012).
- ⁵⁷ A. K. Geim and K. S. Novoselov, *Nat. Mater.* **6**, 183 (2007).
- ⁵⁸ A. H. C. Neto, F. Guinea, N. M. R. Peres, K. S. Novoselov, and A. K. Geim, *Rev. Mod. Phys.* **81**, 109 (2009).
- ⁵⁹ K. S. Novoselov, A. K. Geim, S. V. Morozov, D. Jiang, M. I. Katsnelson, I. V. Grigorieva, S. V. Dubonos, and A. A. Firsov, *Nature* **438**, 197 (2007).
- ⁶⁰ K. Sasaki, S. Murakami, R. Saito, and Y. Kawazoe, *Phys. Rev. B* **71**, 195401 (2005).
- ⁶¹ R. B. Chen, B. J. Lu, C. C. Tsai, C. P. Chang, F. L. Shyu, and M. F. Lin, *Carbon* **42**, 2873 (2004).
- ⁶² M. Szopa, M. Marganska, and E. Zipper, *Phys. Lett. A* **299**, 593 (2002).
- ⁶³ S. K. Maiti, *Physica E* **31**, 117 (2006).
- ⁶⁴ S. K. Maiti, *Solid State Phenom.* **155**, 87 (2009).
- ⁶⁵ S. Bellucci and P. Onorato, *Physica E* **41**, 1393 (2009).
- ⁶⁶ P. A. Orellana and M. Pacheco, *Phys. Rev. B* **71**, 235330 (2005).
- ⁶⁷ L. K. Castelano, G. -Q. Hai, B. Partoens, and F. M. Peeters, *Phys. Rev. B* **78**, 195315 (2008).
- ⁶⁸ P. Dutta, S. K. Maiti, and S. N. Karmakar, *Eur. Phys. J. B* **85**, 126 (2012).
- ⁶⁹ M. P. L. Sancho, M. C. Munoz, and L. Chico, *Phys. Rev. B* **63**, 165419 (2001).
- ⁷⁰ H. Lin, J. Lagoute, V. Repain, C. Chacon, Y. Girard, J. -S. Lauret, F. Ducastelle, A. Looiseau, and S. Rousset, *Nature Mater.* **9**, 235 (2010).
- ⁷¹ S. Sorella and E. Tosatti, *Europhys. Lett.* **19**, 699 (1992).
- ⁷² R. Heyd, A. Charlier, and E. McRae, *Phys. Rev. B* **55**, 6820 (1997).
- ⁷³ R. E. Peierls, *Z. Phys.* **80**, 763 (1933).
- ⁷⁴ K. Wakabayashi, M. Fujita, H. Ajiki, and M. Sigrist, *Phys. Rev. B* **59**, 8271 (1999).
- ⁷⁵ L. Brey and H. A. Fertig, *Phys. Rev. B* **73**, 235411 (2006).
- ⁷⁶ K. Wakabayashi and K. Harigaya, *J. Phys. Soc. Jpn.* **72**, 998 (2003).
- ⁷⁷ J. Fernández-Rossier, *Phys. Rev. B* **77**, 075430 (2008).
- ⁷⁸ Y. Son, M. L. Cohen, and S. G. Louie, *Nature (London)* **444**, 347 (2006).
- ⁷⁹ S. K. Maiti, S. Saha, and S. N. Karmakar, *Eur. Phys. J. B* **79**, 209 (2011).
- ⁸⁰ S. Saha, S. K. Maiti, and S. N. Karmakar, *Eur. Phys. J. B* **85**, 283 (2012).
- ⁸¹ J. Zhong and G. M. Stocks, *Nano Lett.* **6**, 128 (2006).
- ⁸² Y. Cui, X. F. Duan, J. T. Hu, C. M. Lieber, *J. Phys. Chem. B* **104**, 5213 (2000).
- ⁸³ P. Dutta, S. K. Maiti, and S. N. Karmakar, *AIP Conf. Proc.* **1536**, 581 (2013).
- ⁸⁴ P. Dutta, S. K. Maiti, and S. N. Karmakar, *Phys. Lett. A* **367**, 1567 (2012).
- ⁸⁵ S. K. Maiti, *Nanotechnol. Rev.* **1**, 255 (2012).
- ⁸⁶ S. Bellucci and P. Onorato, *Physica E* **41**, 1393 (2009).
- ⁸⁷ S. Bellucci and P. Onorato, *Eur. Phys. J. B* **73**, 215 (2010).
- ⁸⁸ E. L. Pankratov and E. A. Bulaeva, *Rev. Theor. Sci.* **1**, 58 (2013).
- ⁸⁹ M. Lipkind, *Rev. Theor. Sci.* **1**, 145 (2013).
- ⁹⁰ S. Celasun, *Rev. Theor. Sci.* **1**, 319 (2013).
- ⁹¹ M. Ibrahim and H. Elhaes, *Rev. Theor. Sci.* **1**, 368 (2013).
- ⁹² N. A. Zimbovskaya, *Rev. Theor. Sci.* **2**, 1 (2014).
- ⁹³ P. Di Sia, *Rev. Theor. Sci.* **2**, 146 (2014).